Punjab University Journal of Mathematics (2025), 57(07), 757-789
https://doi.org/10.52280/pujm.2025.57(07)04

Modeling Micromagnetorotational Dynamics in Magneto-Micropolar Fluids with Thermal Relaxation Effects

Received
27 May, 2025

Revised
04 November, 2025

Accepted
26 November, 2025

Published Online
17 December, 2025

*Atif Ali Zafar
Department of Mathematics, Capital University of Science and Technology Islamabad, Pakistan

Saba Ashfaq
Department of Mathematics, Bilquis Post Graduate College for Women, PAF Nur Khan Base, Rawalpindi, Pakistan

Mahnoor Asif
Department of Mathematics, University of Poonch Rawalakot, Kahuta-Haveli Campus, Azad Kashmir, Pakistan

Hadia Parveen
Department of Mathematics, National University of Modern Languages, Islamabad, Pakistan

Abstract. Conventional models of magneto-micropolar fluids often overlook the complexities of anisotropic particle rotation and depend on the physically restrictive Fourier's law, which assumes instantaneous heat transport. To overcome these limitations, the present study comprehensively investigates the boundary-layer flow of a magneto-micropolar fluid by integrating two key physical mechanisms: the anisotropic Micromagnetorotation (MMR) constitutive relation and the Cattaneo–Christov (CC) heat-flux model accounting for thermal relaxation. The resulting nonlinear governing partial differential equations are solved numerically using the shooting method. The findings reveal that the MMR parameter exerts a dual influence—broadening the momentum boundary layer while thinning the thermal boundary layer. Moreover, the inclusion of the CC model introduces a physically consistent correction by predicting a measurable reduction in the local Nusselt number relative to the classical Fourier formulation. The outcomes of this research provide fundamental insights essential for the accurate modeling, design, and optimization of microcooling systems and magnetic nanoparticle transport technologies.

AMS (MOS) Subject Classification Codes: 35S29; 40S70; 25U09
Key Words: Cattaneo–Christov model; Micromagnetorotation; micropolar fluids; bound-

**Corresponding Author*: zafaratifali@gmail.com; zafaratifali56@gmail.com

ary layer flow; magnetohydrodynamics; stretching sheet; shooting method; magnetic induction.

1. Introduction

A micropolar fluid is one that exhibits microscopic effects arising from the local structure and micromotion of fluid elements. Such fluids consist of rigid macromolecules that possess independent translational and rotational motions. Their effectiveness appears in applications such as liquid crystals, lubricants, and biological fluids flowing through narrow capillaries. The development of micropolar fluid theory traces its origins to the pioneering contributions of the Cosserat brothers (1909), and was later formalized by Eringen [8, 9]. This formulation extends beyond the classical Newtonian paradigm by permitting suspended particles to undergo microrotations independently of their translational motion [11]. In parallel to these developments, modern studies on generalized non-Newtonian fluids have further enriched the theoretical landscape; for instance, an analytical investigation of Casson fluid flow over a Riga plate using the Prabhakar fractional derivative has highlighted how fractional-order constitutive laws can significantly influence boundary-layer behavior [19].

Several notable investigations have enriched the understanding of micropolar fluid dynamics in various boundary layer flows. Bhattacharyya et al. [20] and Gamar et al. [13] analysed flows over shrinking and stretching sheets, respectively. Naveen et al. [23] examined the effects of activation energy and the Biot number on radiative micropolar fluid flow, and Khan and Hameed [18] presented a detailed examination of electrically induced magnetic flow in a channel. More recently, Abdelgaber et al. [2] explored the combined effects of magnetic field, thermal radiation, and chemical reaction on micropolar fluid flow over a stretching sheet, while Vaishnav et al. [30] investigated radiative micropolar fluid motion over a curved stretching surface, emphasizing viscous dissipation and chemical effects. Furthermore, Ghiya and Tiwari [16] examined anisotropic porosity effects on electroosmotic micropolar flow within a wavy channel, highlighting the need to move beyond isotropic formulations to accurately capture micro–macro rotational (MMR) dynamics. In addition, Ye et al. [32] presented a mathematical analysis offering global strong solutions to three-dimensional nonhomogeneous magneto-micropolar fluid equations with density-dependent viscosity, reaffirming that coupled MHD–micropolar systems continue to represent an active frontier in theoretical and applied fluid mechanics research. Together, these studies demonstrate both the sustained analytical depth and the expanding multidimensional relevance of micropolar fluid modeling in modern boundary-layer and magnetohydrodynamic contexts.

Magnetohydrodynamics (MHD) constitutes the field of science concerned with the behavior of electrically conducting fluids subjected to magnetic fields. MHD is essential for controlling these fluids, as the induced Lorentz forces significantly influence motion. Eringen [10] explored the MHD characteristics of micropolar fluids, and recent numerical work continues to show how magnetic fields affect velocity, temperature, and microrotation profiles in boundary layer flows [28]. A highly specialized and increasingly critical aspect of magnetic fluid dynamics is Micromagnetorotation (MMR). MMR arises in systems where suspended magnetic particles induce simultaneous fluid rotation and translation, profoundly altering velocity and microrotation profiles [7]. MMR is vital for applications requiring improved mixing, transport, and thermal control in boundary layer flows. However, early models often relied on isotropic assumptions for magnetization. In a crucial recent advancement, Khan and Isma [17] presented a magneto-micropolar boundary layer flow model, explicitly demonstrating the necessity of employing an anisotropic constitutive relation to accurately capture these complex MMR dynamics, moving beyond earlier isotropic assumptions.

Building upon these foundations, Magnetohydrodynamic (MHD) effects have continued to play a central role in controlling and optimizing modern nanofluid and bio-convective systems by coupling electromagnetic forces with fluid motion. Earlier works demonstrated that MHD significantly alters microrotation, heat dissipation, and boundary-layer formation in micropolar fluids [29]. Studies systematically integrated MHD with the Cattaneo–Christov non-Fourier heat and mass flux framework, providing a more realistic representation of relaxation-based energy and species transport [26, 15, 12, 33]. These investigations revealed that magnetic fields effectively suppress flow velocity, control nanoparticle suspension, and regulate microorganism distributions, contributing to improved thermal management and process stability. Beyond theoretical advancements, the biomedical relevance of MHD in magnetic hyperthermia and targeted drug delivery [24], as well as its industrial utility in biofuel processing [1], underscores its interdisciplinary importance. Moreover, incorporating computational and ANN-based models has improved prediction of nonlinear MHD-coupled systems [4], advancing intelligent simulation and design of magnetically controlled nanofluidic processes. In this context, neural-computing-based methodologies have also shown strong potential; for example, a recent study employed an intelligent neural framework to analyze the flow and thermal characteristics of ternary hybrid nanofluids over wedge geometries, demonstrating enhanced predictive accuracy for highly nonlinear MHD–thermal systems [6].

The Cattaneo–Christov heat conduction model was developed to address fundamental shortcomings in the classical theory of heat transfer. In his seminal 1822 work, Joseph Fourier proposed a law assuming that heat flux responds instantaneously to temperature gradients, leading to a parabolic heat equation. A major drawback of Fourier's law is its implication of an infinite thermal signal propagation speed, which is physically unrealistic. To overcome this limitation, Cattaneo (1948) modified Fourier's law by introducing a thermal relaxation time, thereby transforming the parabolic heat equation into a hyperbolic form that ensures finite thermal wave speeds. Physically, the thermal relaxation time represents the interval required for the heat flux to adjust to an imposed temperature gradient, allowing thermal disturbances to propagate at a finite speed. Despite this advancement, Cattaneo's model lacked frame invariance, rendering it inconsistent with the principles of continuum mechanics. To address this, Christov (2009) incorporated an upper-convected Oldroyd derivative into Cattaneo's formulation, thus ensuring objectivity and frame invariance. The resulting Cattaneo–Christov heat conduction model offers a more accurate and physically consistent description of thermal transport, particularly in high-frequency and non-equilibrium systems.

Numerous researchers have employed this framework to study viscoelastic fluids, nanofluids, micropolar fluids, Williamson nanofluids, micropolar dusty fluids, and Reiner–Rivlin fluids. More recently, Sadiq et al. [27] investigated thermal distribution in micropolar fluids, showing that energy dissipation increases with the Eckert number and decreases for larger thermal relaxation times. Fatima et al. [14] analyzed three-dimensional micropolar flows with motile microorganisms over permeable surfaces, while Nayak et al. [22] examined free convection in micropolar nanofluids under inertial drag and chemical reactions. Agbaje et al. [3] explored free convection in micropolar hybrid nanofluids with irregular heat sources and sinks, and Reddy et al. [25] studied Darcy–Forchheimer radiative flow containing gyrotactic microorganisms. Almutairi [5] conducted a bioconvective thermal analysis of radiative micropolar nanofluids, while Lone et al. [21] investigated the combined influence of magnetization, radiation, and porosity. In addition to these physical advancements, numerical developments have also contributed significantly; for example, the application of cubic B-spline functions within a Galerkin finite-element framework has proven effective for solving complex sub-diffusion equations, offering improved accuracy and stability for generalized transport models [31].

Despite these parallel and crucial advancements, a significant research gap remains in their unified application. While the study by Khan and Isma [17] established the importance of anisotropic MMR dynamics, their model focused purely on the flow and microrotation fields, entirely neglecting the coupled heat transfer mechanism. Conversely, other contemporary studies that incorporate the Cattaneo-Christov heat flux typically rely on the simplified, isotropic assumptions for magnetic effects or do not consider the MMR field at all. Therefore, to date, no published work has rigorously investigated the simultaneous influence of the anisotropic Micromagnetorotation constitutive relation and the non-Fourier Cattaneo–Christov thermal relaxation effect within the context of magneto-micropolar boundary layer flows.

This study fills this gap by presenting the first unified micropolar continuum framework that couples anisotropic MMR dynamics with the Cattaneo–Christov heat flux model. The goal is to develop a rigorous formulation capable of predicting coupled momentum, heat, and microrotation transport when both particle structure (MMR) and thermal relaxation (CC) are significant. The resulting analysis provides foundational insights for designing and optimizing advanced technological systems, including:

- Thermal Management in Microdevices: Controlling heat transfer rates in magnetic fluids for cooling sensitive micro-electronic components.
- Magneto-Rheological (MR) Dampers: Designing next-generation shock absorbers and vibration control systems where rapid, precise control of viscosity and thermal effects.

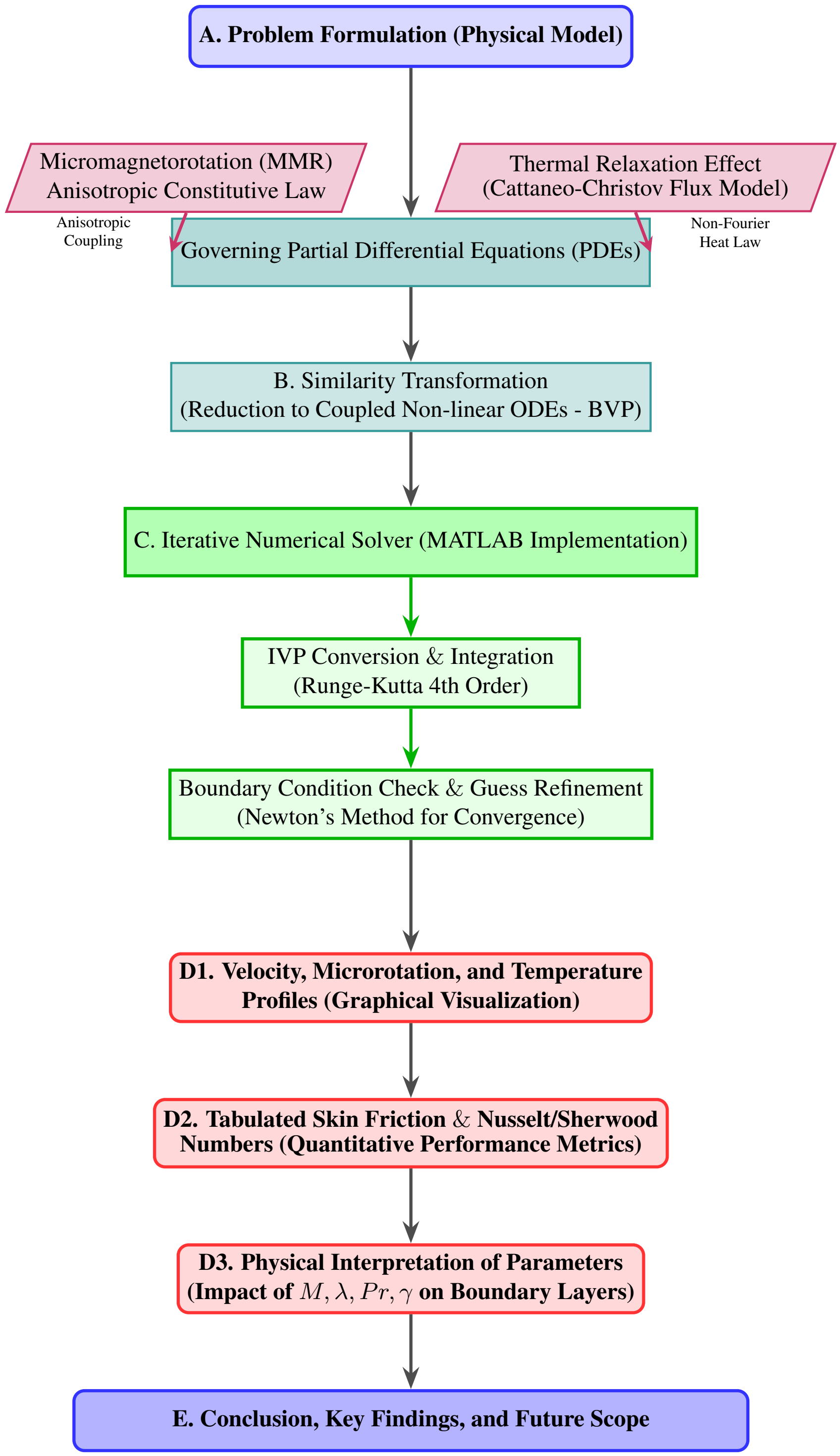

FIGURE 1. Research Framework Flowchart

2. Research Aim

The primary aim of this study is to develop and analyze a unified theoretical and numerical model for magneto-micropolar fluids that simultaneously incorporates anisotropic Micromagnetorotation (MMR) dynamics and the Cattaneo–Christov (CC) thermal relaxation framework. This integration provides a physically realistic description of coupled momentum, heat, and microrotation transfer in boundary-layer flows, enhancing the predictive accuracy of magneto-micropolar modeling for practical engineering applications.

3. Research Objectives

To achieve the stated aim, the present study is guided by the following specific objectives:

(1) To formulate a rigorous two-dimensional steady-state boundary-layer model for a magneto-micropolar fluid that accurately integrates the anisotropic Micromagnetorotation (MMR) constitutive relation.
(2) To incorporate the Cattaneo–Christov (CC) non-Fourier heat flux model into the governing energy equation to capture finite-speed thermal propagation and thermal relaxation effects.
(3) To solve the resulting nonlinear coupled system of equations numerically using the Shooting method and validate the solutions against MATLAB's built-in `bvp4c` solver.
(4) To quantify and interpret the individual and combined effects of key parameters—particularly the MMR parameter (α) and the thermal relaxation time (λ)—on velocity, microrotation, magnetic induction, and temperature fields.
(5) To compare the thermal transport predicted by the CC model with the classical Fourier law through the evaluation of the local Nusselt number.
(6) To provide clear physical insight into how MMR and CC mechanisms influence the design and optimization of micro-cooling devices and magneto-rheological systems.

4. Mathematical Modeling

FIGURE 2 provides a schematic illustration of the physical configuration and coordinate framework related to the stretching sheet scenario. In this setup, the Cartesian axes x and y are oriented along and perpendicular to the sheet, respectively, with u and v denoting the corresponding fluid velocity components. The sheet is modeled as a flat surface undergoing continuous stretching, where the velocity $u(x)$ varies linearly with the horizontal coordinate. This stretching induces a boundary layer flow adjacent to the surface, characterized by sharp gradients in velocity and related physical quantities. The deformation of the velocity field caused by the sheet's motion plays a crucial role in shaping the boundary layer, a process essential to various industrial practices such as polymer sheet production, extrusion technologies, and metallurgical treatments. In this investigation, we focus on a steady, incompressible, two-dimensional laminar magnetohydrodynamic (MHD) flow of a micropolar fluid subjected to an external magnetic field.

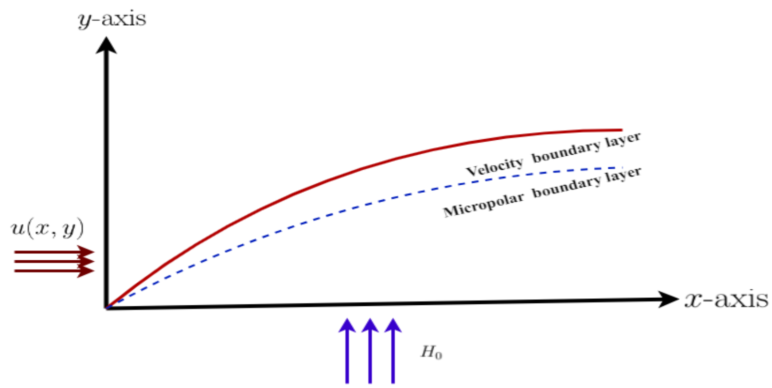

FIGURE 2. The physical geometry.

5. DYNAMICAL DESCRIPTION OF MICROMAGNETOROTATION (MMR)

Under the influence of electromagnetic fields, metallic liquids exhibit micropolar fluid behavior, whereas in the absence of such fields, they may be effectively modeled as Newtonian fluids. The governing equations for conducting metallic liquids were rigorously derived by Shizawa and Tanahashi (1986) through a thermodynamically consistent framework. In the micropolar description, the internal rotations of suspended particles are accounted for, implying that magnetization becomes flow-dependent due to the anisotropic nature of magnetic fluids. Consequently, the magnetization vector cannot generally be assumed to align with the magnetic field vector, necessitating the introduction of a relaxation equation for magnetization. A phenomenological relation for magnetization dynamics was initially proposed by Shliomis (1972); however, his formulation exhibited inconsistencies with Maxwell's equations and lacked full compatibility with the Clausius–Duhem inequality. To resolve these deficiencies, Shizawa and Tanahashi (1986) proposed an alternative approach based on dissipation functions, advocating the removal of the relaxation equation from the governing system. The balance of angular momentum is expressed as:

$$l\left(\frac{dW}{dt} + U \cdot \nabla W\right) = \gamma \nabla^2 W + 4\xi_1(w - W) + M \times H, \tag{5. 1}$$

where $M \times H$ represents the micromagnetorotation (MMR) term, encapsulating the interaction between the magnetization vector and microrotation effects. The comprehensive derivation of the constitutive equation governing magnetization, grounded in thermodynamical principles, can be found in the seminal work of Shizawa and Tanahashi (1986).

$$M = \frac{M_0\left(I - \tau W \cdot \varepsilon\right) \cdot H}{\bar{H}}, \tag{5. 2}$$

where M denotes the magnetization vector, M_0 represents the magnetization strength, I is the identity tensor, and ε signifies the Levis–Civita symbol. Additionally, τ denotes the relaxation time associated with magnetization, H is the external magnetic field, $\bar{H}$ indicates the magnitude of the magnetic field vector, and W corresponds to the microrotation vector characterizing the angular motion of the continuum fluid particles. Following the thermodynamic framework established by Shizawa and Tanahashi (1986), the complete set of governing equations for micropolar continuum paradigm can be recast as follows:

$$\nabla \cdot U = 0, \tag{5. 3}$$

$$\nabla \cdot H = 0, \tag{5. 4}$$

$$\rho\left(\frac{dU}{dt}+U\cdot\nabla U\right) = -\nabla(p)+\xi\nabla^2 U+2\xi_1\nabla\times(W-w)+J\times B+(M\cdot\nabla)H+M\times(\nabla\times H), \tag{5. 5}$$

$$\rho\left(\frac{dH}{dt} + U \cdot \nabla H - H \cdot \nabla U\right) = \xi\nabla^2 H, \tag{5. 6}$$

Here, ρ denotes the fluid density, and H represents the externally applied magnetic field, specified as $H(H_1, H_2, 0)$. By disregarding the effects of fluid angular velocity and electric displacement, Ohm's law admits the following simplified form:

$$w = \nabla \times \frac{U}{2}, \tag{5. 7}$$

$$\nabla \times H = J, \tag{5. 8}$$

$$J = \sigma(E + v \times B), \tag{5. 9}$$

Here, J designates the current density, and σ denotes the electrical conductivity of the medium. The constitutive relation for the magnetic flux density vector is expressed as:

$$B = \mu_0 H + M, \tag{5. 10}$$

where μ_0 represents the magnetic permeability. The energy equation, incorporating joule heating effects, is expressed as:

$$\rho c_p\left(\frac{\partial T}{\partial t} + U.\nabla T\right) = K\nabla^2 T + \frac{J^2}{\sigma} - \nabla.q \tag{5. 11}$$

where, c_p is the specific heat capacity and K is the thermal conductivity of the fluid.
Using the Cattaneo-Christov heat flow model, we discussed the inference of heat transfer in this study. The following expression relates the heat flux and temperature gradient in this model:

$$\mathbf{q} + \lambda_3\left(\frac{\partial \mathbf{q}}{\partial t} + \mathbf{V}\cdot\nabla\mathbf{q} - \mathbf{q}\cdot\nabla\mathbf{V} + (\nabla\cdot\mathbf{V})\mathbf{q}\right) = -K\nabla T, \tag{5. 12}$$

where $\mathbf{q}$ is the heat flux, λ_3 corresponds to heat flux relaxation time, K is the thermal conductivity of the fluid. For $\lambda_3 = 0$, the above equation reduces to Fourier law. Equation (5. 12) reduces to incompressible fluid by applying $\nabla \cdot \mathbf{V} = 0$

$$\mathbf{q} + \lambda_3\left(\frac{\partial \mathbf{q}}{\partial t} + \mathbf{V}\cdot\nabla\mathbf{q} - \mathbf{q}\cdot\nabla\mathbf{V}\right) = -K\nabla T. \tag{5. 13}$$

Equation (5. 1)- (5. 11), which represents the mathematical framework for MHD micropolar fluids, provides a strong theoretical foundation for examining the effects of micromagnetorotation (MMR) in boundary layer flows. Equation (5. 2) presents a constitutive equation for magnetization that is made possible by the addition of the dissipation function. Additionally, equations (5. 7) and (5. 8) provide the constitutive relations governing magnetization dynamics, whereas equation (5. 9) expresses Ohm's law. Equation (5. 8) incorporates Ampère's law, whereas equation (5. 10) provides the constitutive expression for magnetic flux density. The governing equations characterizing the flow field are then derived as follows [17] by using the boundary layer approximations and steady-state assumptions:

$$\frac{\partial u}{\partial x}+\frac{\partial v}{\partial y}=0, \tag{5. 14}$$

$$\frac{\partial H_1}{\partial x}+\frac{\partial H_2}{\partial y}=0, \tag{5. 15}$$

$$\begin{aligned} u\frac{\partial u}{\partial x}+v\frac{\partial u}{\partial y}=\left(\frac{\mu+\xi_1}{\rho}\right)\frac{\partial^2 u}{\partial y^2}-\frac{\sigma}{\rho}\mu_0 H_2^2 u+\frac{2\xi_1}{\rho}\frac{\partial N}{\partial y}+\frac{1}{\rho}\frac{M_0}{\bar{H}}\left(H_1+\tau N H_2\right)\frac{\partial H_1}{\partial x} \\ +\left(H_2-\tau N H_1\right)\frac{\partial H_2}{\partial x}, \end{aligned} \tag{5. 16}$$

$$u\frac{\partial H_1}{\partial x}+v\frac{\partial H_1}{\partial y}=H_1\frac{\partial u}{\partial x}+H_2\frac{\partial u}{\partial y}+\nu_o\frac{\partial^2 H_1}{\partial y^2}, \tag{5. 17}$$

$$u\frac{\partial N}{\partial x}+v\frac{\partial N}{\partial y}=\frac{\gamma^*}{\rho j}\frac{\partial^2 N}{\partial y^2}-\frac{2\xi_1}{\rho j}\left(2N+\frac{\partial u}{\partial y}\right)-M_o H_o \tau H N, \tag{5. 18}$$

Elimination of $\mathbf{q}^*$ from Eqs. (5. 12) and (5. 13) yields to the following single equation for the temperature field:

$$\begin{aligned} u\frac{\partial T}{\partial x}+v\frac{\partial T}{\partial y}=k_\alpha\frac{\partial^2 T}{\partial y^2}+\frac{\sigma}{\rho c_p}H_2^2 u^2-\lambda_3\Bigg[\left(u\frac{\partial u}{\partial x}+v\frac{\partial u}{\partial y}\right)\frac{\partial T}{\partial x}+\left(u\frac{\partial v}{\partial x}+v\frac{\partial v}{\partial y}\right)\frac{\partial T}{\partial y} \\ +u^2\frac{\partial^2 T}{\partial x^2}+v^2\frac{\partial^2 T}{\partial y^2}+2uv\frac{\partial^2 T}{\partial x\partial y}\Bigg] \end{aligned} \tag{5. 19}$$

subjected to the boundary conditions:

$$\begin{cases} u=cx, \quad v=0, \quad \dfrac{\partial H_1}{\partial y}=H_2=0, \quad N=-N_0\dfrac{\partial u}{\partial y}, \quad T=T_w \quad \text{at} \quad y=0, \\ u=ax, \quad H_1=H_e(x)=H_0 x, \quad N\to 0, \quad T\to T_\infty \quad \text{as} \quad y\to\infty. \end{cases} \tag{5. 20}$$

The similarity transformations employed for the non-dimensionalization of the governing model are prescribed as follows:

$$\begin{cases} u=cxf'(\xi), \quad v=-\sqrt{\nu c}f(\xi), \quad \theta(\xi)=\dfrac{T-T_\infty}{T_w-T_\infty}, \quad \xi=\sqrt{\dfrac{c}{\nu}}y, \\ N=cx\sqrt{\dfrac{c}{\nu}}g(\xi), \quad H_1=H_0 x h'(\xi), \quad H_2=-H_0\sqrt{\dfrac{\nu}{c}}h(\xi). \end{cases} \tag{5. 21}$$

The transformation prescribed in (5. 21) culminates in the formulation of the following boundary value problem:

$$(1+K)\frac{\partial^3 f}{\partial \xi^3}-\left(\frac{R_m}{R_e}\right)h^2\frac{\partial f}{\partial \xi}+2K\frac{\partial g}{\partial \xi}+\left(\frac{\alpha}{Re}\right)\left(\frac{\partial h}{\partial \xi}\right)^2-\beta gh\frac{\partial h}{\partial \xi}-\left(\frac{\partial f}{\partial \xi}\right)^2+f\frac{\partial^2 f}{\partial \xi^2}=0, \tag{5. 22}$$

$$\lambda^*\frac{\partial^3 h}{\partial \xi^3}-h\frac{\partial^2 f}{\partial \xi^2}+f\frac{\partial^2 h}{\partial \xi^2}=0, \tag{5. 23}$$

$$\left(1+\frac{K}{2}\right)\frac{\partial^2 g}{\partial \xi^2}-\beta^*\left(2g+\frac{\partial^2 f}{\partial \xi^2}\right)-\tau g-\frac{\partial f}{\partial \xi}g+f\frac{\partial g}{\partial \xi}=0. \tag{5. 24}$$

$$K^*\frac{d^2\theta}{d\xi^2}+f\frac{d\theta}{d\xi}+\left(\frac{R_m}{Re}\right)Ech^2\left(\frac{df}{d\xi}\right)^2-\lambda\left(f\frac{df}{d\xi}\frac{d\theta}{d\xi}+f^2\frac{d^2\theta}{d\xi^2}\right)=0. \tag{5. 25}$$

Boundary conditions in (5. 20) reduces to

$$f=0,\quad \frac{\partial f}{\partial \xi}=1,\quad h=0,\quad \frac{\partial^2 h}{\partial \xi^2}=0,\quad g=-N_0\frac{\partial^2 f}{\partial \xi^2},\quad \theta(\xi)=1 \quad \text{at} \quad \xi=0,$$
$$\frac{\partial f}{\partial \xi}=\frac{a}{c},\quad \frac{\partial h}{\partial \xi}=1,\quad g=0,\quad \theta(\xi)=0 \quad \text{as} \quad \xi\to\infty. \tag{5. 26}$$

The various dimensionless parameters emerging in equations (5. 22)- (5. 25) are defined as follows:

$$K=\frac{\xi_1}{\mu},\ \frac{R_m}{R_e}=\frac{\sigma\mu_o H_0^2\nu}{\rho c^2},\ R_e=\frac{v_0 L}{\nu},\ \alpha=\frac{M_o H_0^2}{\bar{H}},\ \lambda^*=\frac{\nu_o}{\nu},\ \beta^*=\frac{2\xi_1}{\rho j c},\ K^*=\frac{k_\alpha}{\nu},$$
$$\gamma^*=\left(\mu+\frac{\xi_1}{2}\right)j,\ \beta=\frac{M_o H_o^2\tau}{\rho c\bar{H}},\quad \tau=\frac{M_o H_o\tau H}{c},\quad Ec=\frac{c^2x^2}{c_p(T_w-T_\infty)},\quad \lambda=\lambda_3 c. \tag{5. 27}$$

The parameters of principal physical interest, namely the skin-friction coefficient and the Nusselt number, are defined as follows:

$$C_f=\frac{\tau_w}{\rho u_w^2},\quad Nu=\frac{xq_w}{k(T_w-T_\infty)}, \tag{5. 28}$$

where $u_w=cx$ denotes the characteristic velocity, and τ_w represents the wall shear stress, defined as:

$$\tau_w=\left[(\mu+k)\frac{\partial u}{\partial y}+kN\right]\Bigg|_{y=0},\quad q_w=k\frac{\partial T}{\partial y}. \tag{5. 29}$$

Substituting the similarity transformations from (5. 21) into (5. 29), the expressions for the skin-friction coefficient and the local Nusselt number, as defined in (5. 28), can be reformulated as:

$$C_f Re_x^{1/2}=(1+K)\frac{d^2 f}{d\xi^2}(0)+Kg(0),\quad \frac{Nu}{Re_x^{1/2}}=\frac{d\theta}{d\xi}(0), \tag{5. 30}$$

where $Re_x=\frac{u_w x}{\nu}$ is the local Reynolds number.

6. SOLUTION FRAMEWORK

The shooting method, which makes use of the fourth-order Runge-Kutta approach, is used to compute the numerical solutions. The system of ODEs (5. 22), (5. 23), and (5. 24) has been solved by considering the following notations as a first step:

$$f(\xi)=T_1,\ \frac{df}{d\xi}=\frac{dT_1}{d\xi}=T_2,\ \frac{d^2f}{d\xi^2}=\frac{dT_2}{d\xi}=T_3,\ \frac{d^3f}{d\xi^3}=\frac{dT_3}{d\xi},\ h(\xi)=T_4,$$
$$\frac{dh}{d\xi}=\frac{dT_4}{d\xi}=T_5,\ \frac{d^2h}{d\xi^2}=\frac{dT_5}{d\xi}=T_6,\ \frac{d^3h}{d\xi^3}=\frac{dT_6}{d\xi},\ g(\xi)=T_7,\ \frac{dg}{d\xi}=T_8,\ \frac{d^2g}{d\xi^2}=\frac{dT_8}{d\xi}.$$

The system of equations (5. 22), (5. 23) and (5. 24) can be represented in the form of the following first-order coupled ODEs:

$$\frac{dT_1}{d\xi}=T_2, \qquad T_1(0)=0,$$

$$\frac{dT_2}{d\xi}=T_3, \qquad T_2(0)=1,$$

$$\frac{dT_3}{d\xi}=\frac{1}{1+K}\left[\left(\frac{R_m}{Re}\right)T_4^2T_2-2KT_8-\left(\frac{\alpha}{Re}\right)T_5^2+\beta T_7T_4T_5+T_2^2-T_1T_3\right],\ T_3(0)=r,$$

$$\frac{dT_4}{d\xi}=T_5, \qquad T_4(0)=0,$$

$$\frac{dT_5}{d\xi}=T_6, \qquad T_5(0)=s,$$

$$\frac{dT_6}{d\xi}=\frac{1}{\lambda^*}[T_4T_3-T_1T_6], \qquad T_6(0)=0,$$

$$\frac{dT_7}{d\xi}=T_8, \qquad T_7(0)=-N_0(r),$$

$$\frac{dT_8}{d\xi}=\frac{1}{\left(1+\frac{K}{2}\right)}\left[\beta^*(2T_7+T_3)+\tau_2T_7+T_2T_7-T_1T_8\right], \qquad T_8(0)=t,$$

The far field boundary condition, represented as $\xi\to\infty$ and specified as $\xi_\infty=10$, must have a suitable finite value after the boundary value problem (BVP) has been transformed into an initial value problem (IVP). The values for $T_3(0)$, $T_5(0)$, and $T_8(0)$ are then needed for the solution. Nevertheless, these figures are not given before the calculation. It is decided that $T_3(0)=r$, $T_5(0)=s$, and $T_8(0)=t$ are the missing initial conditions. After that, a numerical solution is obtained using the fourth-order Runge-Kutta method. In order to improve the first guess, the missing requirements must be selected so that;

$$\left.\begin{aligned} T_2(r,s,t)-A^*=0,\\ T_5(r,s,t)-1=0,\\ T_7(r,s,t)=0,\end{aligned}\right\} \tag{6. 31}$$

Newton's method has been used to solve the algebraic equation (6. 31) numerically. This formula has the following itreative form:

$$\begin{bmatrix} r\\ s\\ t\end{bmatrix}_{(n+1)} = \begin{bmatrix} r\\ s\\ t\end{bmatrix}_{(n)} \begin{bmatrix} \frac{\partial T_2}{\partial r} & \frac{\partial T_2}{\partial s} & \frac{\partial T_2}{\partial t}\\ \frac{\partial T_5}{\partial r} & \frac{\partial T_5}{\partial s} & \frac{\partial T_5}{\partial t}\\ \frac{\partial T_7}{\partial r} & \frac{\partial T_7}{\partial s} & \frac{\partial T_7}{\partial t}\end{bmatrix}_{(n)} \begin{bmatrix} T_2 - A^*\\ T_5 - 1\\ T_7 - 0\end{bmatrix}_{(n)}$$

To successfully iterate the above formula, we need the following new notations:

$$\begin{aligned}
&\frac{\partial T_1}{\partial r} = T_9,\ \frac{\partial T_2}{\partial r} = T_{10},\ \frac{\partial T_3}{\partial r} = T_{11},\ \frac{\partial T_4}{\partial r} = T_{12},\ \frac{\partial T_5}{\partial r} = T_{13},\ \frac{\partial T_6}{\partial r} = T_{14},\\
&\frac{\partial T_7}{\partial r} = T_{15},\ \frac{\partial T_8}{\partial r} = T_{16},\ \frac{\partial T_1}{\partial s} = T_{17},\ \frac{\partial T_2}{\partial s} = T_{18},\ \frac{\partial T_3}{\partial s} = T_{19},\ \frac{\partial T_4}{\partial s} = T_{20},\\
&\frac{\partial T_5}{\partial s} = T_{21},\ \frac{\partial T_6}{\partial s} = T_{22},\ \frac{\partial T_7}{\partial s} = T_{23},\ \frac{\partial T_8}{\partial s} = T_{24},\ \frac{\partial T_1}{\partial t} = T_{25},\ \frac{\partial T_2}{\partial t} = T_{26},\\
&\frac{\partial T_3}{\partial t} = T_{27},\ \frac{\partial T_4}{\partial t} = T_{28},\ \frac{\partial y_5}{\partial t} = T_{29},\ \frac{\partial T_6}{\partial t} = T_{30},\ \frac{\partial T_7}{\partial t} = T_{31},\ \frac{\partial T_8}{\partial t} = T_{32}.
\end{aligned}$$

The Newton's iterative technique takes on the following form, as a result of the above notations:

$$\begin{bmatrix} r\\ s\\ t\end{bmatrix}_{(n+1)} = \begin{bmatrix} r\\ s\\ t\end{bmatrix}_{(n)} \begin{bmatrix} T_{10} & T_{18} & T_{26}\\ T_{13} & T_{21} & T_{29}\\ T_{15} & T_{23} & T_{31}\end{bmatrix}_{(n)} \begin{bmatrix} T_2 - A^*\\ T_5 - 1\\ T_7 - 0\end{bmatrix}_{(n)}.$$

To find the missing derivatives present in the Newton formula, the following initial value problem, will have to be tackled.

$$\frac{dT_9}{d\xi} = T_{10}, \qquad T_9(0) = 0,$$

$$\frac{dT_{10}}{d\xi} = T_{11}, \qquad T_{10}(0) = 0,$$

$$\begin{aligned}\frac{dT_{11}}{d\xi} = \frac{1}{1+K}\Bigg[&\left(\frac{R_m}{Re}\right)2T_4T_{12}T_{10} - 2KT_{16} - \left(\frac{\alpha}{Re}\right)2T_5T_{13}\\ &+ \beta(T_{15}T_4T_5 + T_7T_{12}T_5 + T_7T_4T_{13}) + 2T_2T_{10} - T_1T_{11} - T_9T_3\Bigg],\ T_{11}(0) = 1,\end{aligned}$$

$$\frac{dT_{12}}{d\xi} = T_{13}, \qquad T_{12}(0) = 0,$$

$$\frac{dT_{13}}{d\xi} = T_{14}, \qquad T_{13}(0) = 0,$$

$$\frac{dT_{14}}{d\xi} = \frac{1}{\lambda^*}[T_4T_{11} + T_{12}T_3 - T_1T_{14} - T_9T_6], \qquad T_{14}(0) = 0,$$

$$\frac{dT_{15}}{d\xi} = T_{16}, \qquad T_{15}(0) = -N_0,$$

$$\frac{dT_{16}}{d\xi} = \frac{1}{\left(1+\frac{K}{2}\right)}\Bigg[\beta^*(2T_{15}+T_{11})+\tau_2T_{15}+T_2T_{15}+T_{10}T_7-T_1T_{16}-T_9T_8\Bigg],\ T_{16}(0) = 0,$$

$$\frac{dT_{17}}{d\xi} = T_{18}, \qquad T_{17}(0) = 0,$$
$$\frac{dT_{18}}{d\xi} = T_{19}, \qquad T_{18}(0) = 0,$$
$$\frac{dT_{19}}{d\xi} = \frac{1}{1+K}\left[\left(\frac{R_m}{Re}\right)2T_4T_{20}T_{18} - 2KT_{24} - \left(\frac{\alpha}{Re}\right)2T_5T_{21} + \beta(T_{23}T_4T_5 + T_7T_{20}T_5 + T_7T_4T_{21}) + 2T_2T_{18} - T_1T_{19} - T_{17}T_3\right], \quad T_{19}(0) = 0,$$
$$\frac{dT_{20}}{d\xi} = T_{21}, \qquad T_{20}(0) = 0,$$
$$\frac{dT_{21}}{d\xi} = T_{22}, \qquad T_{21}(0) = 1,$$
$$\frac{dT_{22}}{d\xi} = \frac{1}{\lambda^*}[T_{20}T_3 + T_4T_{19} - T_{17}T_6 - T_1T_{22}], \qquad T_{22}(0) = 0,$$
$$\frac{dT_{23}}{d\xi} = T_{24}, \qquad T_{23}(0) = 0,$$
$$\frac{dT_{24}}{d\xi} = \frac{1}{\left(1+\frac{K}{2}\right)}\left[\beta^*(2T_{23}+T_{19})+\tau_2T_{23}+T_{18}T_7+T_2T_{23}-T_{17}T_8-T_1T_{24}\right], T_{24}(0) = 0,$$
$$\frac{dT_{25}}{d\xi} = T_{26}, \qquad T_{25}(0) = 0,$$
$$\frac{dT_{26}}{d\xi} = T_{27}, \qquad T_{26}(0) = 0,$$
$$\frac{dT_{27}}{d\xi} = \frac{1}{1+K}\left[\left(\frac{R_m}{Re}\right)2T_4T_{28}T_{26} - 2KT_{32} - \left(\frac{\alpha}{Re}\right)2T_5T_{29} + \beta(T_{31}T_4T_5 + T_7T_{28}T_5 + T_7T_4T_{29}) + 2T_2T_{26} - T_{25}T_3 - T_1T_{27}\right], \quad T_{27}(0) = 0,$$
$$\frac{dT_{28}}{d\xi} = T_{29}, \qquad T_{28}(0) = 0,$$
$$\frac{dT_{29}}{d\xi} = T_{30}, \qquad T_{29}(0) = 0,$$
$$\frac{dT_{30}}{d\xi} = \frac{1}{\lambda^*}[T_{28}T_3 + T_4T_{27} - T_{25}T_6 - T_1T_{30}], \qquad T_{30}(0) = 0,$$
$$\frac{dT_{31}}{d\xi} = T_{32}, \qquad T_{31}(0) = 0,$$
$$\frac{dT_{32}}{d\xi} = \frac{1}{\left(1+\frac{K}{2}\right)}\left[\beta^*(2T_{31}+T_{27})+\tau_2T_{31}+T_{26}T_7+T_2T_{31}-T_{25}T_8-T_1T_{32}\right], T_{32}(0) = 1.$$

Following stopping criteria is used for Newtons's method:

$$\max\left\{\left|T_2\left(\xi_\infty, r, s, t\right) - A^*\right|, \left|T_5\left(\xi_\infty, r, s, t\right) - 1\right|, \left|T_7\left(\xi_\infty, r, s, t\right)\right|\right\} < 10^{-7},$$

Until the necessary convergence requirements are satisfied, the iterative procedure is continued with the step size set to 0.005. The computed solutions against the skin friction coefficient are shown in TABLE 1. The results reveal that the skin friction coefficient values obtained from the implemented code exhibit excellent agreement with those derived using MATLAB's built-in bvp4c function, thereby validating the accuracy and reliability of the numerical approach. A similar approach will be taken with equation (5. 25).

7. RESULTS AND DISCUSSION

While transforming the governing partial differential equations (PDEs) describing the fluid flow into a system of ordinary differential equations (ODEs), several crucial parameters emerge. TABLE 3 presents the computed values of skin friction and the Nusselt number for various parameter settings. The effects of physical parameters on the distributions of hydrodynamic velocity $f'(\xi)$, microrotational velocity $g(\xi)$, magnetic induction $h'(\xi)$, and temperature gradient $\theta'(\xi)$ are thoroughly analyzed through graphical representations. The results of this study are discussed in detail, along with the significance and interpretation of the influence of each parameter. TABLE 2 provides the validation of the numerical results, confirming the accuracy of the adopted numerical technique.

The decreasing hydrodynamic velocity profiles for various Reynolds number (Re) values are depicted in FIGURE 3, taking into account varied magnetization parameter values. The relative importance of viscous forces or extrinsic influences (such magnetization or resistive drag) in regulating the flow behavior increases as Re rises, despite the fluid's inertial forces tending to increase. This leads to a suppression of the fluid motion, especially near the boundary, resulting in a diminished velocity gradient and a flattened velocity profile. Essentially, at higher Reynolds numbers in this setup, the fluid exhibits reduced hydrodynamic activity due to the dominant damping forces, causing a deceleration in the flow. This behavior reflects a transition towards a more stabilized and slower-moving fluid domain under the influence of increasing Re.

FIGURE 4 illustrates the diminishing hydrodynamic velocity profile with increasing values of the magnetic Reynolds number (R_m). This behavior arises from the complex interplay between the magnetic field and the fluid motion. As R_m increases, magnetic advection intensifies, leading to stronger induced magnetic fields within the fluid. These, in turn, generate substantial Lorentz forces that resist the motion of conducting fluid particles. The resulting electromagnetic damping effect suppresses the velocity gradient, particularly near the boundary layer, thereby flattening the velocity profile. Such a trend is characteristic of magnetohydrodynamic (MHD) flows, where magnetic influences dominate over inertial effects, significantly altering the overall fluid dynamics and promoting flow stabilization.

FIGURE 5 demonstrates the effect of the micromagnerotation (MMR) parameter (α) on the hydrodynamic velocity profile. As the value of α increases, the rotational activity of the microstructural particles within the fluid becomes more significant. This enhanced micromagnerotation facilitates stronger momentum coupling between fluid layers, thereby reducing internal resistance and boosting the overall flow velocity. Consequently, the hydrodynamic boundary layer expands, indicating an increase in velocity gradients near the wall region. The presence of intensified rotational motion not only accelerates the fluid near the surface but also promotes more efficient transport mechanisms. Such behavior is particularly relevant in microfluidic systems and magnetically responsive flows, where control over flow characteristics is essential for optimizing performance.

In the context of magneto-micropolar boundary layer models, the macrorotational velocity profile $g(\xi)$ holds significant importance, as it captures the bulk rotational behavior of the fluid, particularly under the influence of micromagnerotation (MMR) effects. FIGURE 6 presents a non-monotonic trend in this profile with respect to increasing Reynolds number (Re). Initially, near the stretching plate, $g(\xi)$ exhibits a decline as Re increases—an effect primarily attributed to the growing dominance of inertial forces that suppress rotational motion in the near-wall region. This suppression is due to the rapid acceleration of fluid particles, which hinders the development of rotational dynamics close to the boundary. However, further away from the surface, the influence of MMR effects becomes more pronounced, and the rotational characteristics of the flow begin to assert themselves. This results in a reversal in the macrorotational velocity profile, highlighting a distinct transition from an inertia-dominated regime near the wall to a rotation-governed domain in the outer boundary layer. This nuanced behavior underscores the complex interplay between translational inertia and microstructural rotation in magneto-micropolar flows.

FIGURE 7 explores the influence of the micropolar constant (K) on the magnetic induction profile within the magneto-micropolar fluid framework. As K increases, the magnetic induction profile exhibits a significant upward trend. Physically, a higher value of K reflects a stronger coupling between the microrotational motion of microelements and the macroscopic flow field. This enhanced coupling facilitates more efficient momentum and vorticity transfer across fluid layers, which in turn amplifies the interaction between the fluid motion and the imposed magnetic field. The increased microrotation leads to stronger induced currents, thereby intensifying the magnetic induction through enhanced Lorentz force feedback. Consequently, the system exhibits greater magnetic activity, especially in regions where rotational effects are dominant. This behavior highlights the critical role of micropolar interactions in modifying electromagnetic responses in complex fluid systems.

FIGURE 8 illustrates the impact of the magnetic Reynolds number (R_m) on the magnetic induction profile. As R_m increases, a noticeable rise in the magnetic induction profile is observed, along with a corresponding expansion in the magnetic boundary layer. Physically, a higher R_m signifies stronger magnetic advection relative to diffusion, enabling the convected magnetic field lines to be more effectively carried by the fluid flow. This results in an enhanced induction effect, where the interaction between the moving conductive fluid and the magnetic field becomes more pronounced. The strengthened coupling promotes the generation and sustenance of induced magnetic fields, thereby increasing the overall magnetic activity within the fluid domain. The thickening of the boundary layer further reflects the extended influence of magnetic forces in the flow field, characteristic of high-R_m magnetohydrodynamic regimes.

FIGURE 9 highlights the effect of the micromagnerotation (MMR) parameter on the temperature distribution within the fluid. As the value of the MMR parameter increases, a noticeable decline in the temperature profile is observed, along with a corresponding reduction in the thermal boundary layer thickness. This behavior is primarily attributed to the enhanced rotational activity of microstructural elements, which increases internal energy dissipation through microrotational motion. Such rotational dynamics disrupt thermal energy buildup and facilitate more efficient energy transport away from the heated surface.

As a result, the fluid retains less heat, leading to steeper temperature gradients and thinner thermal boundary layers. The intensified micromagnetic interactions thus play a critical role in promoting convective heat transfer, making the system more thermally responsive in the presence of higher MMR effects.

In FIGURE 10, it is evident that an increase in the Eckert number (Ec) results in a rise in fluid temperature. This behavior can be attributed to the conversion of kinetic energy into internal thermal energy within the fluid. At higher Ec values, the viscous dissipation effects become more pronounced, meaning that a greater portion of the fluid's mechanical energy is transformed into heat. This internal heat generation enhances the overall thermal energy content of the system, thereby elevating the temperature distribution throughout the flow field. As a result, increasing Ec intensifies the heating effect, which is particularly relevant in high-speed or high-viscosity flows where thermal energy generation due to viscous effects cannot be neglected.

FIGURE 11 elucidates the influence of the magnetic Reynolds number (R_m) on the temperature distribution $\theta(\xi)$. It is clearly observed that increasing R_m leads to a noticeable rise in fluid temperature. Physically, a higher R_m implies stronger magnetic advection, resulting in more intense interaction between the magnetic field and the moving conductive fluid. This interaction amplifies the Lorentz force, which resists fluid motion and generates additional internal friction. The resulting increase in viscous dissipation contributes to greater thermal energy generation within the fluid. Furthermore, the dampening of convective transport due to magnetic field effects reduces the removal of heat from the boundary layer region. These combined mechanisms enhance thermal accumulation, thereby elevating the overall temperature profile. This behavior highlights the critical role of magnetic field dynamics in modulating heat transfer characteristics in magnetohydrodynamic flows.

FIGURE 12 illustrates the influence of the thermal relaxation time parameter (λ) on the temperature distribution $\theta(\xi)$. It is evident that as λ increases, the temperature profile also rises. Physically, a larger thermal relaxation time implies that the heat flux does not respond instantaneously to temperature gradients. This delayed thermal response, modeled through generalized non-Fourier heat conduction theories such as the Cattaneo-Christov framework, results in a temporary accumulation of thermal energy near the heated boundary. Consequently, the conduction process becomes less efficient in dissipating heat, leading to higher local fluid temperatures and a thicker thermal boundary layer. Such behavior has been reported in several studies involving microstructured fluids and high-frequency thermal processes, underscoring the significance of thermal relaxation effects in modulating heat transfer dynamics.

FIGURE 13 effectively illustrates the dependence of the local convective heat transfer rate, represented by the Nusselt number (Nu), on the Eckert number (Ec) and a kinematic viscosity coefficient (ξ) for the specified flow conditions (including $Re = 10.0$). The Eckert number quantifies the significance of viscous dissipation, the process by which kinetic energy is converted into internal heat due to fluid friction. The parameter ξ serves as a spatial coordinate capturing the development of the flow and thermal boundary layers along the domain. The plot clearly demonstrates that Nu decreases significantly with increasing ξ, particularly evident from the closely packed isolines in the region $0 \leq \xi \lesssim 2$, characteristic of a rapid drop in heat transfer within the thermal entrance region as the boundary layer thickens. Further downstream ($\xi \gtrsim 2$), the decrease in Nu with ξ becomes more gradual as the boundary layer development slows. Simultaneously, the plot shows that for any given ξ, Nu decreases as Ec increases. This is because greater viscous dissipation at higher Ec generates more internal heat within the boundary layer, thereby reducing the temperature difference between the surface and the fluid and diminishing the driving potential for heat transfer. Furthermore, the influence of Ec on Nu appears more pronounced in the entrance region (ξ small) where overall heat transfer rates are higher. Thus, the figure comprehensively captures how viscous dissipation and kinematic viscosity coefficient collectively govern the local convective heat exchange, highlighting the dominant entrance effects and the attenuating role of viscous heating.

FIGURE 14 illustrates the dependence of the local convective heat transfer rate, represented by the Nusselt number Nu, on the Magnetic Reynolds number Re_m and a kinematic viscosity ξ in an MHD fluid flow. The Magnetic Reynolds number quantifies the significance of magnetic field advection by the fluid relative to magnetic diffusion, indicating how strongly the fluid motion influences the magnetic field structure. The plot reveals two primary effects: Firstly, increasing the Magnetic Reynolds number (higher Re_m) generally leads to an increase in the Nusselt number, suggesting that stronger magnetic field advection enhances the heat transfer rate at the boundary, likely by favorably altering the flow or thermal boundary layer structure. This enhancement appears more pronounced in the thermal entrance region (small ξ). Secondly, the plot shows a significant decrease in Nu as the ξ increases. This rapid reduction in Nu for small ξ (the entrance region) transitions to a more gradual decrease further downstream as the thermal boundary layer thickens, increasing the thermal resistance at the wall. Thus, the figure succinctly demonstrates the competing effects of magnetic field interaction (enhancing heat transfer, especially in the entrance) and spatial boundary layer growth (reducing heat transfer with distance) on the overall convective heat exchange.

In the FIGURE 15, the streamlines originate near the lower-left corner ($\xi \approx 0, \eta \approx 0$) and sweep upwards and towards the right. The streamlines near $\eta = 0$ at small ξ are somewhat spread out vertically. As they move towards larger ξ, they curve upwards and become more horizontal. The streamlines spread out vertically across the domain, indicating that the fluid reaches relatively higher η values as it flows downstream. The spacing between the streamlines changes, suggesting variations in velocity magnitude throughout the flow field.

In FIGURE 16, the isotherms originate near the lower-left corner ($\xi \approx 0, \eta \approx 0$), where presumably the boundary is heated or cooled. They extend outwards and towards the right, curving as they develop along the ξ direction. The isotherms penetrate relatively far into the fluid in the η direction as ξ increases, indicating that the region affected by the wall temperature (the thermal boundary layer) is relatively thick. The isotherms appear less steep near the $\eta = 0$ boundary for a given ξ, suggesting a relatively smaller temperature gradient at the wall.

Compared to the $K = 0.5$ case, the streamlines in FIGURE 17 show a similar general pattern of originating from the lower-left and moving towards the right. However, a notable difference is that the streamlines appear to stay *closer* to the $\eta = 0$ boundary for a longer distance in ξ compared to $K = 0.5$ before curving upwards and spreading out vertically. The overall vertical spread of the streamlines across the domain appears somewhat reduced compared to the $K = 0.5$ case within the depicted range.

Similar to the FIGURE 18 $K = 0.05$ case, the isotherms originate from the lower-left and develop along ξ. However, comparing to $K = 0.05$, the isotherms appear to penetrate less far into the fluid (reach lower maximum η values) at the same ξ. The isotherms near the $\eta = 0$ boundary seem slightly steeper than in the $K = 0.05$ case, indicating a somewhat larger temperature gradient at the wall. The thermal boundary layer appears thinner than for $K = 0.05$.

In FIGURE 19, the tendency of the streamlines to hug the $\eta = 0$ boundary is even more pronounced than in the $K = 1.0$ case. The streamlines remain very close to the lower boundary for a considerable distance in ξ before gradually curving upwards. The vertical spread of the streamlines is the least among the three plots, with the flow field appearing more compressed towards the $\eta = 0$ axis. The streamlines seem more densely packed near the boundary and then spread out more abruptly above.

In FIGURE 20, the isotherms penetrate the least far into the fluid among the three cases. The region of significant temperature variation is confined closer to the $\eta = 0$ boundary. The isotherms near the $\eta = 0$ boundary appear the steepest compared to both $K = 0.05$ and $K = 0.1$ cases, suggesting the largest temperature gradient at the wall for a given ξ. The thermal boundary layer is the thinnest in this case.

FIGURE 21, shows the mesh plot provides a comprehensive visualization of how a critical fluid dynamics outcome, represented here as Z, is influenced by the combined effects of the fluid's micropolar and microrotation characteristics (mapped along the X-axis) and the interplay of inertial and magnetic forces (mapped along the Y-axis). The complex, undulating surface reveals a rich physical landscape where Z does not change uniformly with the influencing parameters. Prominent peaks on the surface signify specific combinations of micropolar/microrotation strengths and inertial/magnetic interactions that lead to a maximization of the outcome Z, while deep valleys indicate conditions causing Z to be minimized. As we navigate this parameter space, varying the balance of forces and material properties along the X and Y directions causes Z to rise and fall, demonstrating a highly sensitive and non-linear response. The presence of numerous oscillations across the surface further highlights the intricate coupling between these fundamental fluid physics phenomena, indicating that subtle adjustments in the governing parameters can lead to significant and sometimes fluctuating changes in the observed outcome Z. Ultimately, this plot maps the complex dependency of a key flow characteristic Z on the synergistic influence of micropolar behavior, fluid inertia, and magnetic field interactions.

FIGURE 22, presents a comprehensive visualization of how a significant fluid dynamics outcome, represented here as Z, is influenced by the combined effects related to the microrotation parameter (α, mapped along the X-axis) and the flow inertia (represented by the Reynolds number (Re), mapped along the Y-axis). The surface reveals a striking physical landscape where Z does not change uniformly with the influencing parameters. Prominent peaks on the surface signify specific combinations of microrotation strengths and inertial forces that lead to a maximization of the outcome Z, while deep valleys indicate conditions causing Z to be minimized. As the influence of the microrotation parameter increases (moving away from the center along the X-axis) or as the flow inertia increases (moving away from the center along the Y-axis), the outcome Z generally decreases from its peak and exhibits complex oscillatory behavior. These oscillations and surrounding valleys signify that changes in the balance between microrotation effects and inertial forces lead to a sensitive and non-linear response in Z, with multiple local extrema across the parameter space. The plot thus effectively maps how the interplay between the fluid's internal rotation characteristics (governed by α) and its tendency to resist changes in motion (governed by Re) collectively shapes a key aspect of the flow behavior, highlighting optimal conditions and regions of complex response.

In FIGURES 23-25, the relationship between a significant fluid dynamics outcome, represented by the surface Z, and the combined effects related to the microrotation parameter (α, mapped along the X-axis) and the fluid inertia (represented by the Reynolds number (Re), mapped along the Y-axis). Across all three plots, the shape of the Z surface remains consistently complex, featuring a prominent peak near the center and surrounding oscillations and valleys. This consistent landscape signifies that the general dependency of this outcome Z on the balance between microrotation effects and inertia follows a predictable, albeit non-linear and sensitive, pattern. The primary visual difference between the figures lies in a label indicating a specific value for the Nusselt number (Nu). While the overall surface mapping Z vs scaled α and Re is the same, the variation in this specific Nu value from figure to figure suggests how the actual heat transfer rate at a particular state changes. This change in the specific Nu value is likely driven by variations in *other* underlying physical parameters of the flow (such as the micropolar constant K, Magnetic Reynolds number (Re_m), or buoyancy terms) which are not explicitly mapped on the axes of this Z surface but influence the overall flow and thermal behavior, leading to different specific heat transfer outcomes even while the fundamental response surface $Z(X, Y)$ maintains its form.

Based on the analysis of the surface plot, FIGURE 26; the skin friction coefficient C_f is shown to be negative over the displayed range of parameters α and β^*. The plot clearly demonstrates that as both α and β^* increase, the value of C_f increases, becoming less negative. This observed trend signifies a decrease in the magnitude of the skin friction $|C_f|$, and consequently, a reduction in the viscous drag exerted on the stretching surface. The parameters α and β^* are characteristic of fluids exhibiting micro-rotational behavior, influencing the internal dynamics and coupling between micro-rotation and translational flow. An increase in these parameters enhances these micro-rotational effects, which typically modifies the velocity profile within the boundary layer near the wall. This modification results in a reduced magnitude of the velocity gradient normal to the wall ($\partial u/\partial y$ at the surface). Since skin friction is directly proportional to this velocity gradient, a reduction in its magnitude leads to a decrease in the magnitude of the shear stress $|\tau_w|$ and thus a lower $|C_f|$, as consistently illustrated by the rising trend of the surface plot towards less negative values.

FIGURE 27 illustrates the combined detrimental influence of viscous dissipation, quantified by the Eckert number (Ec), and the non-instantaneous nature of heat transfer, characterized by the thermal relaxation parameter (λ), on the magnitude of heat transfer from the fluid to the stretching surface. An increase in the Eckert number signifies more significant viscous heating within the fluid, a process converting mechanical energy into thermal energy due to internal friction. This internal temperature rise in the fluid reduces the temperature gradient near the surface, thereby hindering the heat transfer rate towards the boundary. Simultaneously, the thermal relaxation parameter (λ), arising from non-Fourier heat conduction models, introduces a time lag in the heat flux response to temperature gradients and accounts for a finite speed of thermal wave propagation. A larger λ indicates greater thermal inertia, leading to thinner thermal boundary layers and a reduced effective temperature gradient at the surface. Consequently, less heat is transferred. The surface plot clearly visualizes this synergistic reduction: the magnitude of heat transfer (likely the Nusselt number on the vertical axis) decreases noticeably as both Ec and λ increase across the parameter space, thereby confirming that both effects serve to attenuate the thermal exchange between the fluid and the stretching surface.

The surface plot in FIGURE 28 demonstrates that both the thermal relaxation parameter (λ) and the magnetic Reynolds number (R_m) contribute to reducing the magnitude of heat transfer from the fluid to the stretching surface. The parameter λ accounts for the non-instantaneous nature of heat transfer, introducing a time lag in the heat flux response and acknowledging a finite speed for thermal propagation. An increase in λ signifies greater thermal inertia, which typically leads to thinner thermal boundary layers and a consequent reduction in the temperature gradient at the surface, thus hindering heat transfer. The magnetic Reynolds number (R_m) characterizes the significance of magnetic field induction caused by the fluid motion. Higher R_m implies more dominant induced magnetic fields, and their interaction with any applied field generates a Lorentz force that opposes the fluid flow. This magnetic retardation alters the flow and temperature profiles within the boundary layer in a manner that reduces the heat transfer to the surface. The plot, presenting the Nusselt number (Nu), clearly shows that as both λ and R_m increase, the value of Nu decreases (becomes more negative), confirming the reduction in the magnitude of heat transfer from the fluid to the stretching surface. This visual evidence supports the physical understanding that both thermal relaxation and magnetic induction effects suppress thermal energy exchange at the boundary.

TABLE 1. Comparison of results computed by Shooting method and bvp4c function for different values of R_m

R_m	Shooting method	`bvp4c`
0.1	−1.093766118	−1.093766118
0.3	−1.105556912	−1.105556912
0.5	−1.114758305	−1.114758305
0.7	−1.122278555	−1.122278555

TABLE 2. Grid Validation Results

ξ	Grid_200	Grid_500	Grid_1000	Grid_2000
1	0.544301496446947	0.544310901013703	0.54472589872948	0.544726479153752
2	0.736452394345661	0.736450730317131	0.73876679824494	0.73876615207457
4	1.25895155325598	1.25895154925533	1.26727459916062	1.26727321213043
6	2.22931806804484	2.22931182698431	2.24133971131576	2.24133822129108
8	3.80906194727772	3.80906193954189	3.82254075506123	3.8225398774001

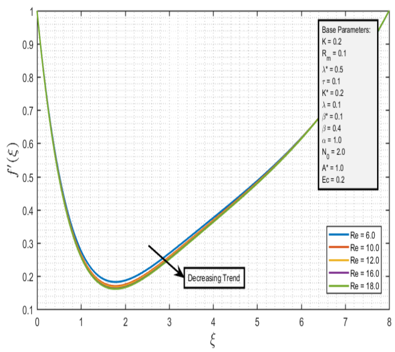

FIGURE 3. Effect of Re on $f'(\xi)$

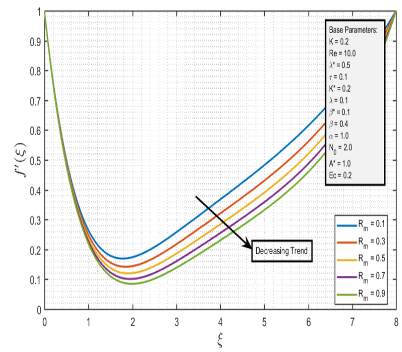

FIGURE 4. Effect of R_m on $f'(\xi)$

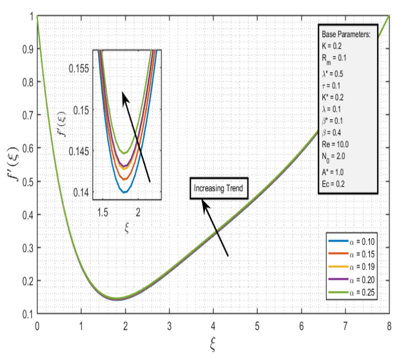

FIGURE 5. Effect of α on $f'(\xi)$

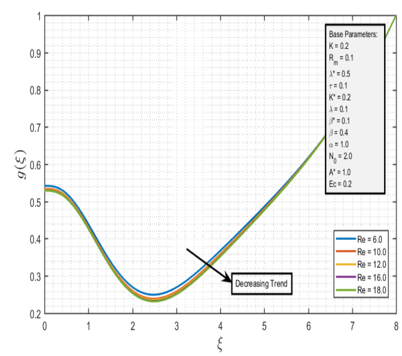

FIGURE 6. Effect of Re on $g(\xi)$

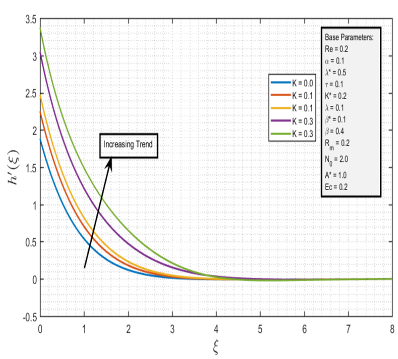

FIGURE 7. Effect of K on $h'(\xi)$

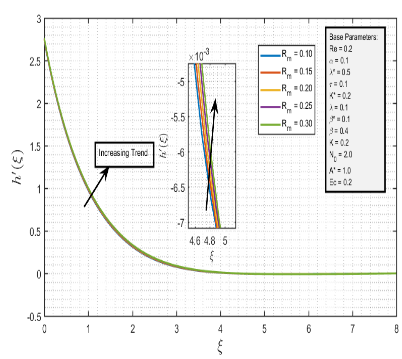

FIGURE 8. Effect of R_m on $h'(\xi)$

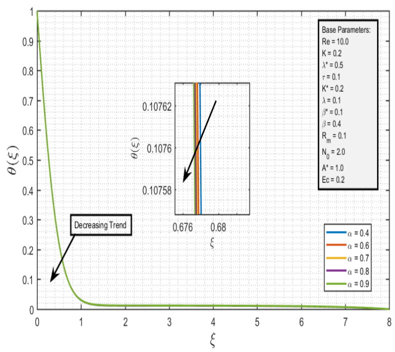

FIGURE 9. Effect of α on $\theta(\xi)$

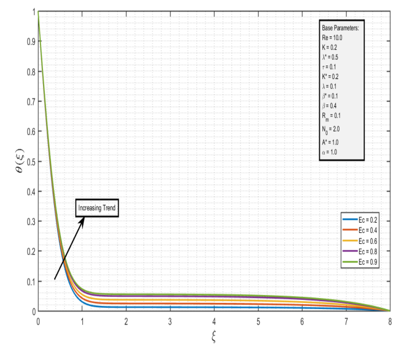

FIGURE 10. Effect of Ec on $\theta(\xi)$

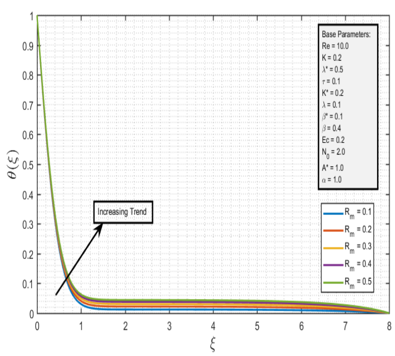

FIGURE 11. Effect of R_m on $\theta(\xi)$

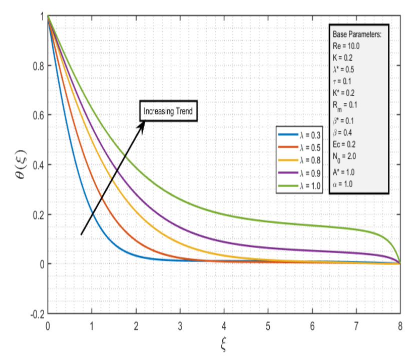

FIGURE 12. Effect of λ on $\theta(\xi)$

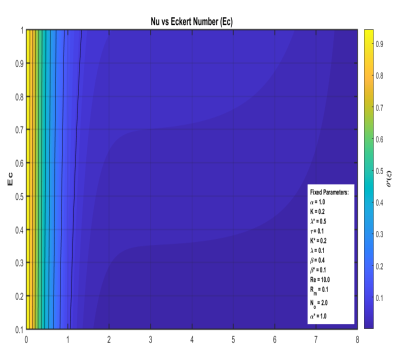

FIGURE 13. Effect of Ec on Nu

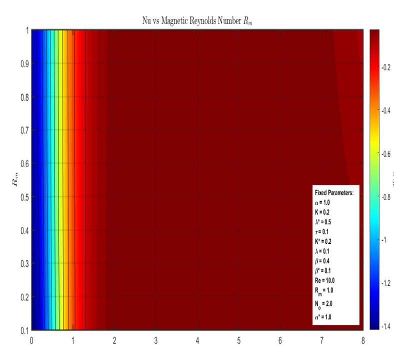

FIGURE 14. Effect of R_m on Nu

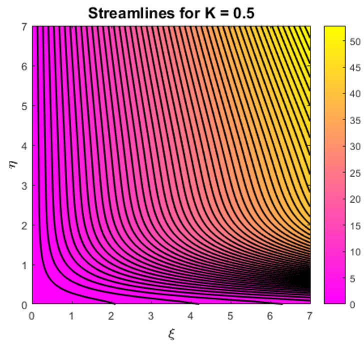

FIGURE 15. Streamlines for $K = 0.5$

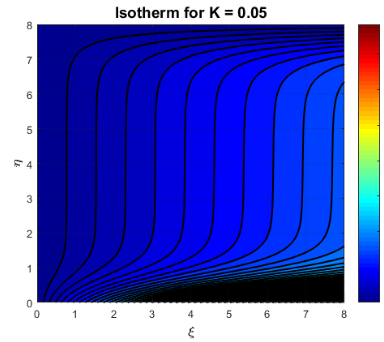

FIGURE 16. Isotherm for $K = 0.05$

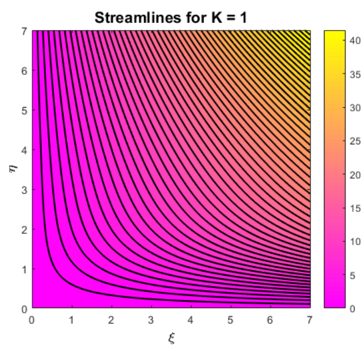

FIGURE 17. Streamlines for $K = 1$

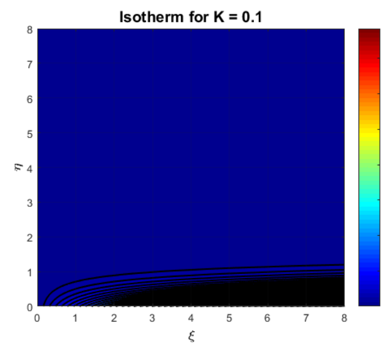

FIGURE 18. Isotherm for $K = 0.1$

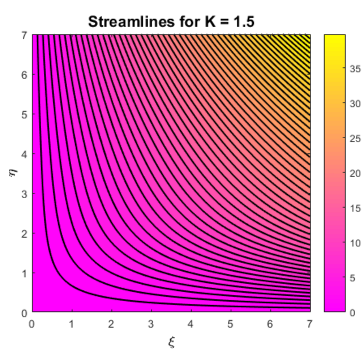

FIGURE 19. Streamlines for $K = 1.5$

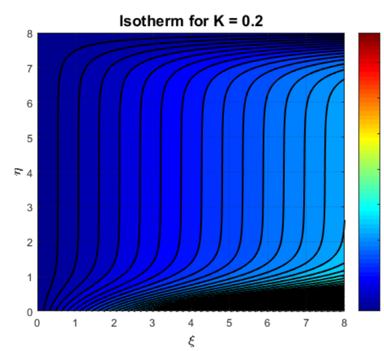

FIGURE 20. Isotherm for $K = 0.2$

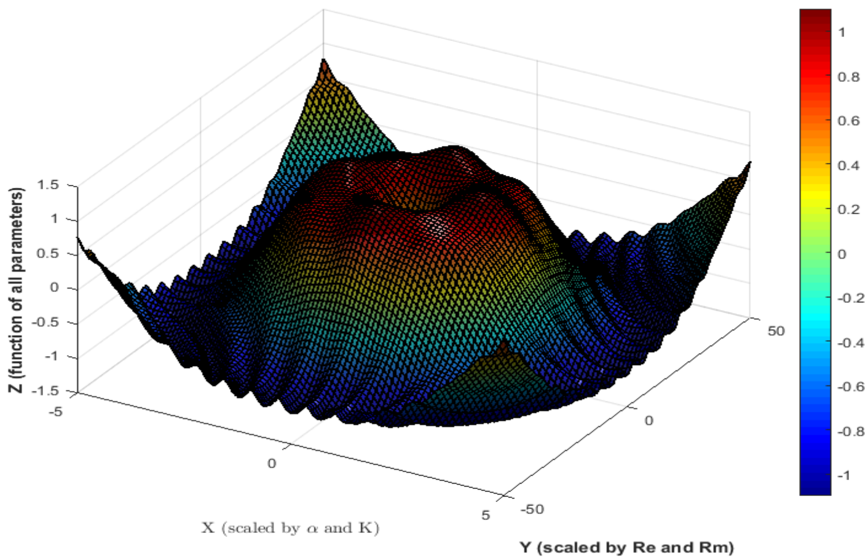

FIGURE 21. Mesh Plot of Z as a function of X and Y

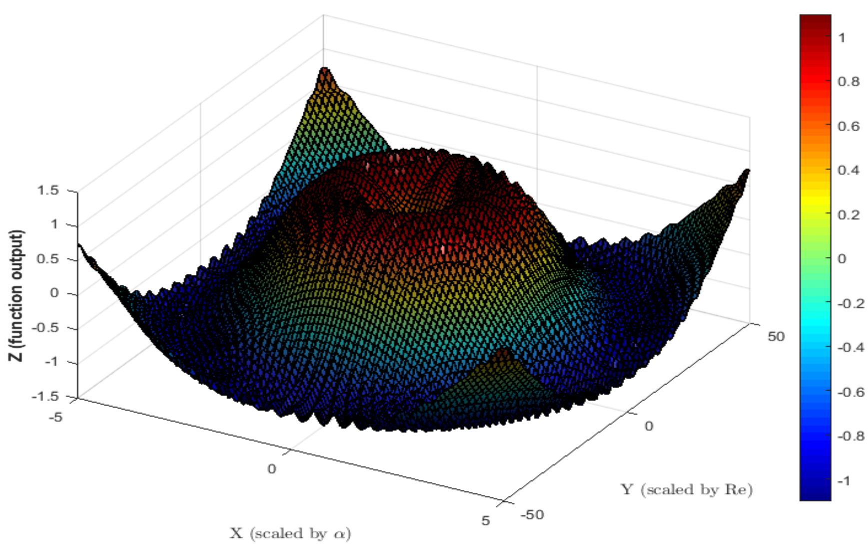

FIGURE 22. 3D Mesh Plot of the function output Z based on X and Y

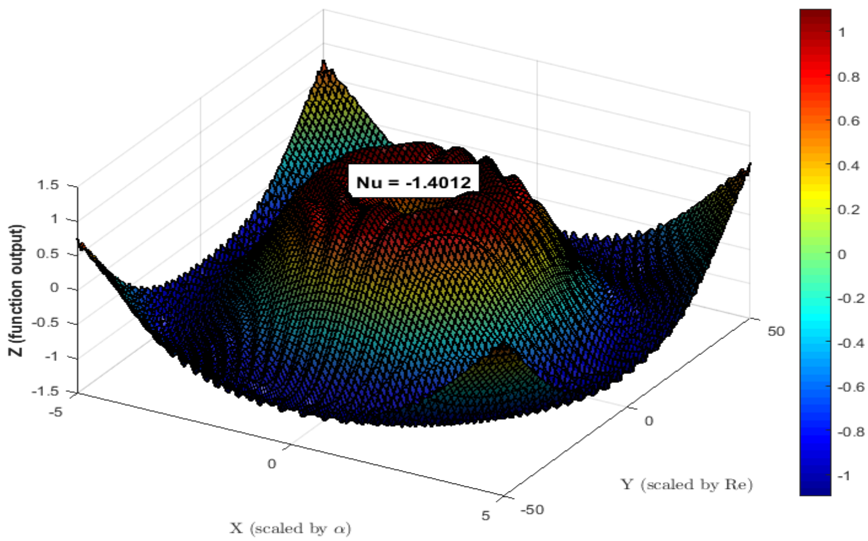

FIGURE 23. 3D Mesh Plot of Z for Nu = -1.4012

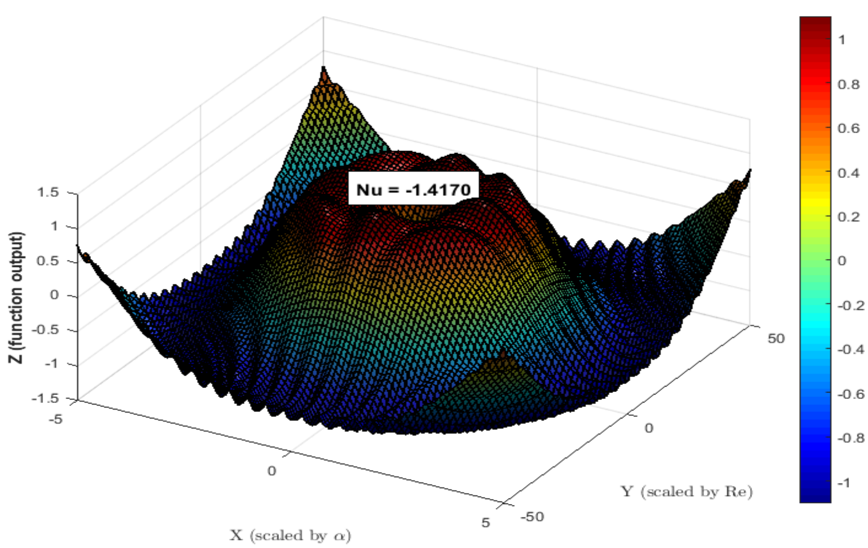

FIGURE 24. 3D Mesh Plot of Z for Nu = -1.4170

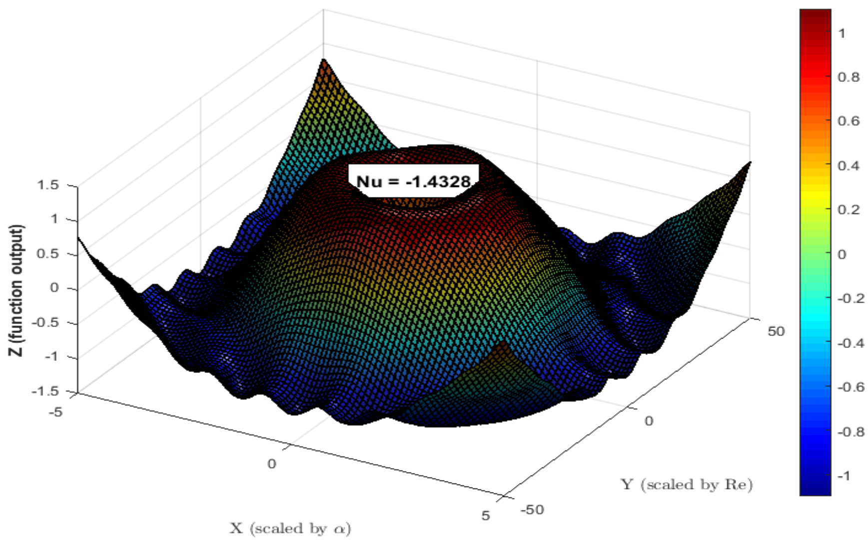

FIGURE 25. 3D Mesh Plot of Z for Nu = -1.4328

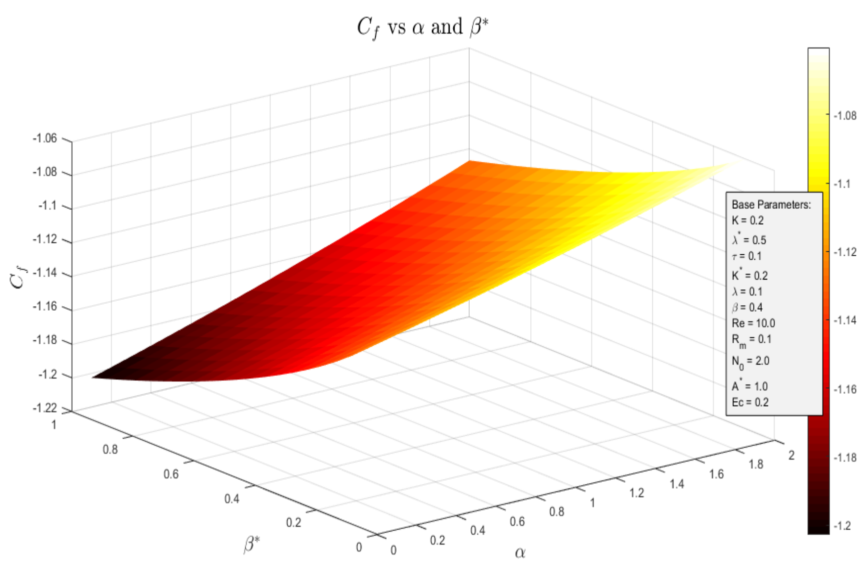

FIGURE 26. A coupling effect of α and β^* on the skin friction of the fluid

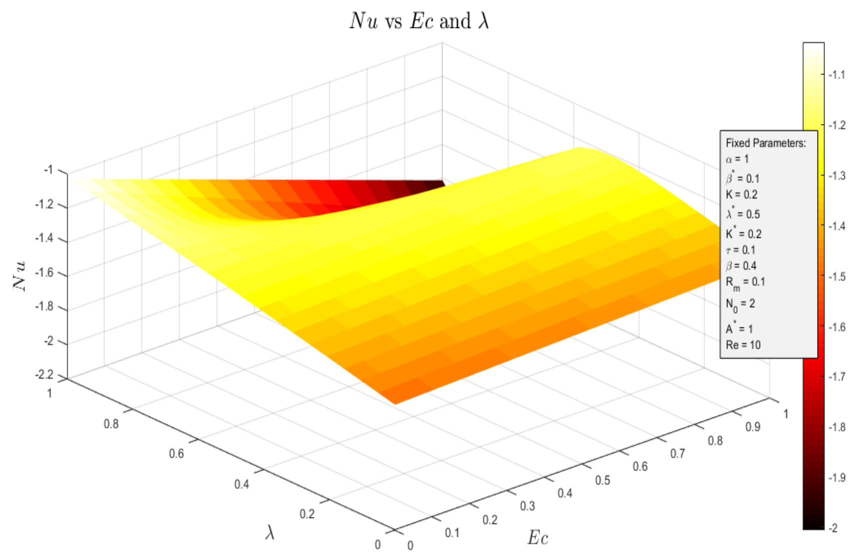

FIGURE 27. A coupling effect of Ec and λ on the Nusselt number of the fluid

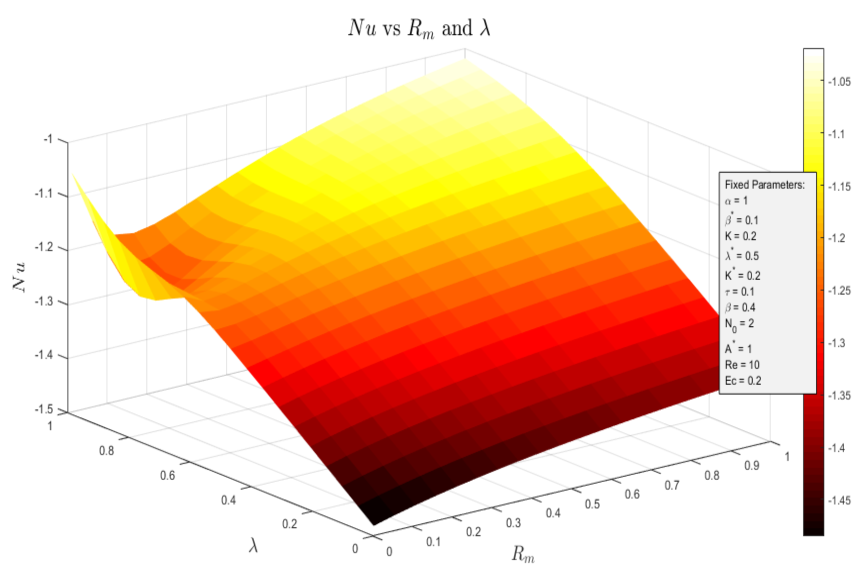

FIGURE 28. A coupling effect of R_m and λ on the Nusselt number of the fluid

TABLE 3. The numerical results of $(Re_x)^{1/2}Cf_x$ and $(Re_x)^{-1/2}Nu_x$.

α	K	λ^*	τ	K^*	λ	β	β^*	Re	R_m	N_0	A^*	Ec	$Re_x^{1/2}C_f$	$Re_x^{-1/2}Nu$
1.0	0.2	0.5	0.1	0.2	0.1	0.4	0.1	10	0.1	2.0	1.0	0.2	-1.093766	-1.429022
0.6	0.2	0.5	0.1	0.2	0.1	0.4	0.1	10	0.1	2.0	1.0	0.2	-1.105769	-1.425324
0.7	0.2	0.5	0.1	0.2	0.1	0.4	0.1	10	0.1	2.0	1.0	0.2	-1.102832	-1.426240
0.8	0.2	0.5	0.1	0.2	0.1	0.4	0.1	10	0.1	2.0	1.0	0.2	-1.099853	-1.427162
1.0	0.05	0.5	0.1	0.2	0.1	0.4	0.1	10	0.1	2.0	1.0	0.2	-0.975332	-1.497602
1.0	0.1	0.5	0.1	0.2	0.1	0.4	0.1	10	0.1	2.0	1.0	0.2	-1.011648	-1.480390
1.0	0.15	0.5	0.1	0.2	0.1	0.4	0.1	10	0.1	2.0	1.0	0.2	-1.050912	-1.458444
1.0	0.2	0.1	0.1	0.2	0.1	0.4	0.1	10	0.1	2.0	1.0	0.2	-1.095575	-1.429974
1.0	0.2	0.2	0.1	0.2	0.1	0.4	0.1	10	0.1	2.0	1.0	0.2	-1.094738	-1.429774
1.0	0.2	0.3	0.1	0.2	0.1	0.4	0.1	10	0.1	2.0	1.0	0.2	-1.094185	-1.429567
1.0	0.2	0.5	0.2	0.2	0.1	0.4	0.1	10	0.1	2.0	1.0	0.2	-1.101742	-1.428669
1.0	0.2	0.5	0.4	0.2	0.1	0.4	0.1	10	0.1	2.0	1.0	0.2	-1.115784	-1.428187
1.0	0.2	0.5	0.5	0.2	0.1	0.4	0.1	10	0.1	2.0	1.0	0.2	-1.122069	-1.428026
1.0	0.2	0.5	0.1	0.0	0.1	0.4	0.1	10	0.1	2.0	1.0	0.2	-1.093766	-2.202157
1.0	0.2	0.5	0.1	0.15	0.1	0.4	0.1	10	0.1	2.0	1.0	0.2	-1.093766	-1.691222
1.0	0.2	0.5	0.1	0.21	0.1	0.4	0.1	10	0.1	2.0	1.0	0.2	-1.093766	-1.388240
1.0	0.2	0.5	0.1	0.2	0.2	0.4	0.1	10	0.1	2.0	1.0	0.2	-1.093766	-1.381403
1.0	0.2	0.5	0.1	0.2	0.3	0.4	0.1	10	0.1	2.0	1.0	0.2	-1.093766	-1.334293
1.0	0.2	0.5	0.1	0.2	0.4	0.4	0.1	10	0.1	2.0	1.0	0.2	-1.093766	-1.288653
1.0	0.2	0.5	0.1	0.2	0.1	0.5	0.1	10	0.1	2.0	1.0	0.2	-1.111425	-1.422472
1.0	0.2	0.5	0.1	0.2	0.1	0.6	0.1	10	0.1	2.0	1.0	0.2	-1.128847	-1.415741
1.0	0.2	0.5	0.1	0.2	0.1	0.7	0.1	10	0.1	2.0	1.0	0.2	-1.146003	-1.408817
1.0	0.2	0.5	0.1	0.2	0.1	0.4	0.2	10	0.1	2.0	1.0	0.2	-1.107108	-1.428180
1.0	0.2	0.5	0.1	0.2	0.1	0.4	0.3	10	0.1	2.0	1.0	0.2	-1.118235	-1.427665
1.0	0.2	0.5	0.1	0.2	0.1	0.4	0.4	10	0.1	2.0	1.0	0.2	-1.127867	-1.427346
1.0	0.2	0.5	0.1	0.2	0.1	0.4	0.1	6	0.1	2.0	1.0	0.2	-1.077304	-1.423378
1.0	0.2	0.5	0.1	0.2	0.1	0.4	0.1	12	0.1	2.0	1.0	0.2	-1.097757	-1.430369
1.0	0.2	0.5	0.1	0.2	0.1	0.4	0.1	18	0.1	2.0	1.0	0.2	-1.104303	-1.432546
1.0	0.2	0.5	0.1	0.2	0.1	0.4	0.1	10	0.2	2.0	1.0	0.2	-1.100068	-1.413032
1.0	0.2	0.5	0.1	0.2	0.1	0.4	0.1	10	0.3	2.0	1.0	0.2	-1.105556	-1.399537
1.0	0.2	0.5	0.1	0.2	0.1	0.4	0.1	10	0.4	2.0	1.0	0.2	-1.110411	-1.387913
1.0	0.2	0.5	0.1	0.2	0.1	0.4	0.1	10	0.1	2.1	1.0	0.2	-1.102920	-1.417233
1.0	0.2	0.5	0.1	0.2	0.1	0.4	0.1	10	0.1	2.12	1.0	0.2	-1.104796	-1.414678
1.0	0.2	0.5	0.1	0.2	0.1	0.4	0.1	10	0.1	2.13	1.0	0.2	-1.105740	-1.413372
1.0	0.2	0.5	0.1	0.2	0.1	0.4	0.1	10	0.1	2.0	1.1	0.2	-1.080437	-1.433823
1.0	0.2	0.5	0.1	0.2	0.1	0.4	0.1	10	0.1	2.0	1.2	0.2	-1.069121	-1.437697
1.0	0.2	0.5	0.1	0.2	0.1	0.4	0.1	10	0.1	2.0	1.3	0.2	-1.059290	-1.440907
1.0	0.2	0.5	0.1	0.2	0.1	0.4	0.1	10	0.1	2.0	1.0	0.1	-1.093766	-1.436964
1.0	0.2	0.5	0.1	0.2	0.1	0.4	0.1	10	0.1	2.0	1.0	0.3	-1.093766	-1.421080
1.0	0.2	0.5	0.1	0.2	0.1	0.4	0.1	10	0.1	2.0	1.0	0.4	-1.093766	-1.413139

8. Research Questions

The following research questions have been formulated to guide the present investigation:

(1) How does the inclusion of anisotropic Micromagnetorotation affect the velocity and microrotation distributions in a magneto-micropolar boundary-layer flow?
(2) What is the impact of incorporating the Cattaneo–Christov thermal relaxation model on the temperature field compared with Fourier's classical heat conduction law?
(3) How do variations in the MMR parameter (α) and the thermal relaxation time (λ) influence the momentum and thermal boundary-layer thicknesses?
(4) In what way do electromagnetic parameters such as the magnetic Reynolds number (R_m) and the micropolar coupling constant (K) alter the flow and heat-transfer behavior?
(5) What are the implications of the observed changes in skin-friction and Nusselt numbers for practical ferrofluidic and micro-thermal management applications?

9. Conclusion

This study successfully formulated, analyzed, and numerically solved a coupled model describing the Micromagnetorotation (MMR) and thermal relaxation dynamics in a magneto-micropolar fluid. All defined objectives were achieved through the development of a comprehensive mathematical framework that simultaneously incorporated the effects of microrotation, magnetohydrodynamics (MHD), and non-Fourier heat conduction via the Cattaneo–Christov (CC) model.

The principal conclusions are summarized as follows:

- Dual Role of Micromagnetorotation (MMR): An increase in the MMR parameter induces a retarding internal couple stress that broadens the velocity boundary layer while simultaneously thinning the thermal boundary layer, demonstrating its dual influence on both momentum and heat transfer.
- Thermal Lag and Relaxation: The inclusion of the Cattaneo–Christov model eliminates the non-physical assumption of infinite heat propagation. Increasing the thermal relaxation parameter (λ) decreases the wall heat transfer rate (local Nusselt number) due to finite-speed thermal diffusion, confirming the physical realism of the model.
- Microrotation Dynamics: The microrotation velocity near the surface decreases with higher MMR strength, implying that enhanced micromagnetization stabilizes the flow by absorbing angular momentum and moderating vorticity.
- Parametric Sensitivities: Higher Reynolds numbers (Re) suppress near-wall motion due to increased inertia, while larger magnetic Reynolds numbers (R_m) strengthen electromagnetic damping. The micromagnetization parameter (α) promotes microstructural rotational activity, and the coupling number (K) reinforces microrotation–magnetic field interactions.
- Energy Generation and Heat Transfer: The Eckert number (Ec) elevates the temperature through viscous dissipation, whereas larger thermal relaxation values reduce the temperature gradient, collectively diminishing the Nusselt number.

- Flow and Thermal Response: Nonlinear and oscillatory trends observed in surface plots highlight the sensitivity of the coupled system to small parameter variations, underscoring the intricate interplay between momentum, microrotation, and electromagnetic effects.

10. Limitations and Future Directions

Although the proposed model provides a unified understanding of MMR and CC mechanisms, several limitations remain that offer promising avenues for future research:

- The present analysis is restricted to two-dimensional, steady-state flow under a uniform magnetic field. Future studies should explore unsteady and three-dimensional configurations with spatially varying magnetic intensities to capture realistic physical behaviors.
- Additional physical phenomena—such as thermal radiation, chemical reactions, variable viscosity, or nonlinear convective heat transport—may be incorporated within the CC–MMR framework to enhance predictive capability.
- The extension of the current model to hybrid nanofluids or bio-micropolar systems could reveal new interdisciplinary applications, particularly in micro-electronic cooling and biomedical flow control.
- Data-driven optimization and machine learning approaches may be employed to identify optimal combinations of control parameters for energy-efficient design of cooling, lubrication, and magnetic fluid systems.

Overall, this research establishes a strong theoretical foundation for understanding the coupled Micromagnetorotation and thermal relaxation phenomena in magneto-micropolar fluids, providing a pathway toward advanced MHD-based technologies in thermal management and smart fluidic devices.

11. Acknowledgment

I would like to express my sincere gratitude to the Punjab University Journal of Mathematics for providing such a supportive and innovative environment, which enabled us to successfully publish our research. On behalf of all the authors, I deeply appreciate the dedicated efforts of the entire journal team. Our special thanks go to Managerial Secretary Ms. Sumaira Hussain, whose timely responses to our queries and consistent guidance throughout the process were immensely helpful.

I am also grateful to all the co-authors for their active participation in our discussions, their commitment to the project, and the valuable new ideas they contributed. Their collective insight enabled us to collaboratively develop the MMR terminology, an area in which very few articles have been published in the existing literature.

We hope that our combined efforts will contribute meaningfully to future research and inspire further exploration in this specialized domain.

12. Authors Contribution

*__Atif Ali Zafar__:- Methodology, Investigation, Validation, Project supervision, Writing-original draft.
Saba Ashfaq:- Conceptualization, Investigation, Validation, Reviewing original draft.

Mahnoor Asif:- Investigation, Validation, Formal analysis, Visualization, Review-editing draft.
Hadia Parveen:- Formal analysis, Visualization.

13. Declarations

Conflict of Interest: The authors declare no competing interests.
Funding: No funding was available for this research.

14. Appendix A:

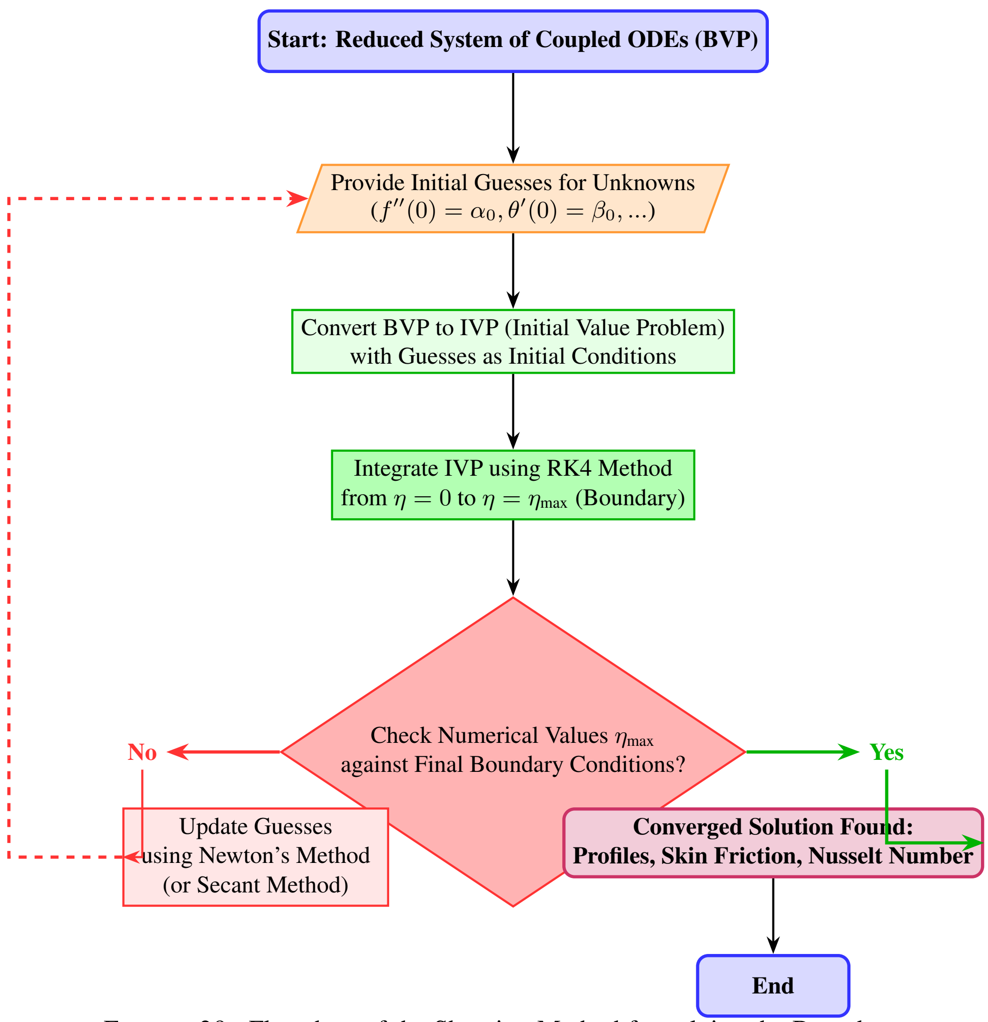

FIGURE 29. Flowchart of the Shooting Method for solving the Boundary Value Problem (BVP)

REFERENCES

[1] M. Abbas, S. M. Shaaban, S. Elaissi, I. Khan, R. F. Rashid, A. A, *Scrutinization of radiation flow of trihybrid nanofluid with Cattaneo–Christov flux model and oxytactic and gyrotactic microbes: A biofuel applications*, Journal of Radiation Research and Applied Sciences. **18**, No.4, (2025) 101920.

[2] K. M. Abdelgaber, M. Fathy, P. K. Abbassi, and R. A. Elbarkoki, *Heat and mass transfer of micropolar fluid flow over a stretching sheet by legendre collocation method*, Scientific Reports. **15**, No.1, (2025) 25921.

[3] T.M. Agbaje, S. Panda, S. R. Mishra, and R. Baithalu, *Free convection of Cattaneo-Christov heat flux model for the micropolar hybrid nanofluid through permeable stretching surface with inertial drag and irregular heat sink/source*, Multiscale and Multidisciplinary Modeling, Experiments and Design. **8**, No.3, (2025) 1-16.

[4] F. Alimi, S. Rehman, M. Bouzidi, F. Asiri, T. Saidani, and V. Tirth, *Numerical and artificial neural network framework for predicating MHD radiative flow and heat transfer of hybrid nanofluid with Cattaneo-Christov theory*, Case Studies in Thermal Engineering. (2025) 106311.

[5] A.D. Almutairi, *Bioconvective thermal estimation of radiative micropolar nanofluid with mass suction and variable Brownian diffusion: Cattaneo–Christov model*, Discover Applied Sciences. **7**, No.1, (2025) 56.

[6] M. I. Asjad, and A. Wahab, *Neural Computing Approach to the Flow and Thermal Analysis of Ternary Hybrid Nanofluid Over Wedges*, Punjab Univ. J. Math., **57**, No.04, (2025) 512-541.

[7] K. E. Aslani, and I. E. Sarris, *Effect of micromagnetorotation on magnetohydrodynamic Poiseuille micropo-lar flow: Analytical solutions and stability analysis*, Journal of Fluid Mechanics **920**, (2021).

[8] E. A. Cemal, *Simple microfluids*, International Journal of Engineering Science. **2**, No. 2, (1964) 205-217.

[9] E. A. Cemal, *Theory of micropolar fluids*, Journal of mathematics and Mechanics. (1966) 1-18.

[10] E. A. Cemal, *Microcontinuum field theories: II. Fluent media*, **2**, (2001)

[11] W. H. Chu, and M-H. CHANG, *Stability of micropolar fluid flow between concentric rotating cylinders*, Journal of Fluid Mechanics. **631**, (2009) 343-362.

[12] U.J.Das, and D. Mali, *Bioconvective MHD flow of hybrid alumina-silver-water nanofluid across a moving needle containing gyrotactic microorganisms with Cattaneo-Christov heat and mass flux model*, Hybrid Advances. **9**, (2025) 100391.

[13] G. Fakhraldeen, M. D. Shamshuddin, M. S. Ram, S. O. Salawu, and E. O. Fatunmbi, *Exploration of thermal radiation and stagnation point in MHD micropolar nanofluid flow over a stretching sheet with Navier slip*, Numerical Heat Transfer, Part A: Applications. **86**, No.17, (2025) 6117-6129.

[14] N. Fatima, A. Majeed, N. Ijaz, R. Ghodhbani, and N. Saleem, *Thermal performance of Cattaneo-Christov heat flux model on 3D micropolar fluid with motile microbes across a permeable surface*, BioNanoScience. **14**, No.3, (2024) 2419-2434.

[15] P. Francis, P. Sambath, S. Noeiaghdam, U. Fernandez-Gamiz, and S. Dinarvand, *Computational analysis of bioconvective MHD hybrid nanofluid flow of non-Newtonian fluid over cone/plate: A study based on the Cattaneo-Christov heat and mass flux model*, Engineering Science and Technology, an International Journal. **63**, (2025) 101970.

[16] N. Ghiya, and A. Tiwari, *Impact of anisotropic porosity on electroosmotic flow of micropolar fluid in wavy channel*, International Journal of Multiphase Flow. (2025) 105444.

[17] M. S. Khan, and I. Hameed, *A New Magneto-Micropolar Boundary Layer Model for Liquid Flows–Effect of Micromagnetorotation (MMR)*, arXiv preprint arXiv:2308.08457. (2023)

[18] M. S. Khan, and I. Hameed, *FreeFEM++ based heat transfer analysis of an electrically induced magnetic flow within the framework of micropolar continuum*, Numerical Heat Transfer, Part A: Applications. **85**, No.18, (2024) 3110-3128.

[19] Z. Khola, M. Abbas, M. Haroon, and M. I. Asjad, *Analytical Investigation of Casson Fluid Flow over a Riga Plate using the Prabhakar Fractional Derivative*, Punjab Univ. J. Math. **57**, No.05, (2025) 559-575.

[20] B. Krishnendu, S. Mukhopadhyay, G. C. Layek, and I. Pop, *Effects of thermal radiation on micropolar fluid flow and heat transfer over a porous shrinking sheet*, International Journal of Heat and Mass Transfer. **55**, No.11-12, (2012) 2945-2952.

[21] S. A. Lone, Z. Raizah, R. Bossly, F. S. Alduais, A. Al-Bossly, and A. Khan, *Thermal Investigation of Water-Based Radiative Magnetized Micropolar Hybrid Nanofluid Flow Subject to Impacts of Cattaneo-Christov Flux Model on a Variable porous Stretching Sheet with Machine Learning Approach*, Chinese Physics B. **34**, No.6, (2025) 064401.

[22] P.P. Nayak, P. Mathur, and S. R. Mishra, *Cattaneo–Christov heat and mass flux on free convection of micropolar nanofluid with inertial drag and chemical reaction*, Multiscale and Multidisciplinary Modeling, Experiments and Design. **8**, No.5, (2025) 1-21.

[23] N. Padiegepati, C. RamReddy, and K. Vajravelu, *Comparative investigation of activation energy and biot number on quadratic convective flow of a radiating micropolar fluid*, Numerical Heat Transfer, Part A: Applications. **85**, No.17, (2024) 2773-2791.

[24] P.K. Pattnaik, R. Baithalu, S. R. Mishra, and S. Panda, *Radiative MHD micropolar nanofluid used in hyperthermia treatment in cancer therapy and targeted drug delivery systems*, Thermal Advances. (2025) 100064.

[25] M. V. Reddy, R. Meenakumari, J. M. Nath, T. K. Das, and C. Sagar, *Darcy-Forchheimer radiative flow of micropolar nanofluid with Cattaneo-Christov heat flux featuring gyrotactic microorganisms*, Radiation Effects and Defects in Solids. (2025) 1-27.

[26] S. B. Reddy, C. Janaiah, and R. S. Raju, *Double Cattaneo-Christov diffusion effects on radiating three dimensional MHD Nanofluid flow past an exponentially stretching sheet with Multiple Slip effects*, Journal of Radiation Research and Applied Sciences. **18**, No. 3, (2025) 101800.

[27] M. N. Sadiq, B. Sarwar, M. Sajid, and N. Ali, *Heat transfer in unsteady separated stagnation point flow of a micro-polar fluid: Cattaneo–Christov model*, Journal of Thermal Analysis and Calorimetry. **147**, No. 8, (2022) 5199-5209.

[28] S. Sharma, A. Dadheech, A. Parmar, J. Arora, Q. Al-Mdallal, and S. Saranya, *MHD micro polar fluid flow over a stretching surface with melting and slip effect*, Scientific reports. **13**, No.1, (2023) 10715.

[29] P. Srilatha, A. M. Hassan, B. S. Goud, and E. R. Kumar, *Mathematical Study of MHD micropolar fluid flow with radiation and dissipative impacts over a permeable stretching sheet: Slip effects phenomena*, Frontiers in Heat and Mass Transfer. **21**, (2023) 539-562.

[30] B. K. Vaishnav, S. Choudhary, P. Choudhary, K. Jat, K. Loganathan, and S. Eswaramoorthi, *Computational analysis of radiative micropolar fluid flow over a curved stretching sheet with viscous dissipation*, Discover Applied Sciences. **7**, No. 5, (2025) 451.

[31] A. Yasin, M. K. Iqbal, and M. Abbas, *Application of Cubic B-Spline Functions in Galerkin Finite Element Method for Solving Second Order Sub-Diffusion Equation*, Punjab Univ. J. Math., **57**, No. 04, (2025) 491-511.

[32] X. Ye, Y. Zhou, and M. Zhu, *Global strong solutions to the 3D nonhomogeneous incompressible magneto-micropolar fluid equations with density-dependent viscosity*, Nonlinear Analysis: Real World Applications. **88**, (2026) 104477.

[33] H. Zeb, K. Shah, M. Alqudah, and T. Abdeljawad, *Variable thermal conductivity effects on MHD flow of non-Newtonian ternary hybrid nanofluid between rotating disks, A Cattaneo–Christov heat transfer analysis*, Case Studies in Thermal Engineering. **71**, (2025) 106119.